Annals of Nuclear Energy 152 (2021) 107974

Contents lists available at ScienceDirect

Annals of Nuclear Energy

journal homepage: www.elsevier.com/locate/anucene

Zero-power noise up to 100 kHz in the IPEN/MB-01 research reactor facility

Diogo Feliciano dos Santos, Adimir dos Santos *

Instituto de Pesquisas Energéticas e Nucleares, Av. Lineu Prestes 2242 CEP: 05508-000, São Paulo, SP, Brazil

ARTICLE INFO

Article history:
Received 15 April 2020
Received in revised form 27 September 2020
Accepted 20 October 2020
Available online 19 November 2020

Keywords:
Reactor noise
APSD measurements
Two-region two-group kinetic model
Subcritical reactivity
Neutron generation time
Neutron lifetime

ABSTRACT

Subcritical noise experiments at frequencies up to 100 kHz employing two distinct boron dilution in the reactor tank water (286.8 and 578.6 ppm of natural boron) were performed in the IPEN/MB-01 reactor. The Auto Power Spectral Densities (APSD) were inferred employing the IPEN/MB-01 Correlator and were best described by a four-mode decay model up to about 70 kHz. The analyses reveal that the first two modes were related to thermal neutron and the other two to the fast ones. The coupling between thermal and fast neutrons was weak, and they could be considered uncoupled. A two-region two-group kinetic model was built and for the first time important parameters, such as the subcritical reactivities, generation times, and the prompt neutron decay constants all in the core and reflector in the 286.8 ppm case were inferred. The experiments can be considered unique of its kind and the theory/experiment comparisons reached good agreements.

1. Introduction

Subcritical measurement techniques are considered an open area in the Reactor Physics field. The techniques used to determine subcritical reactivity can be classified into three categories: 1) Static or quasi-static methods, 2) Dynamic methods, and 3) Neutron noise methods. The static or quasi-static methods rely mostly on the detector signals placed strategically around or inside of the reactor core. The reactor system is considered at steady-state and the detector responses, mainly counts, are collected for further analyses. The main assumption is that detector count rates are linked to subcritical levels, and, consequently, count rate variations are linked to reactivity variation between two configurations. This is the main hypothesis for the development of the Source Multiplication Method (Blaise et al., 2011; Tsuji et al., 2003). This is the simplest method to measure the subcritical reactivity from the three categories. The dynamic method is based on the analysis of the time response of detectors placed in the reactor after a source neutron pulse. The technique assumes that the point kinetics can represent the neutron population evolution over time after a neutron pulse (considered as a Dirac peak). The Area method (also referred to as the Sjöstrand method) (Sjöstrand, 1956) allows one to determine straightforwardly the reactivity (in units of dollar) of a subcritical nuclear reactor with no input from theoretical calculations. Examples of utilization of this technique may be found in ref. (Mihalczo et al., 1990). The neutron noise method (de Hoffmann, 1949; Feynman et al., 1956; Moore, 1959; 1958a; 1958b;; Orndoff, 1957; Saito, 1979; Uhrig, 1970; Williams, 1974) is based on the macroscopic and microscopic noise acquisitions in the reactor system. The macroscopic noise occurs when ensembles of neutrons are detected, as in ionization chamber current or the counts of a pulse mode detector. The count rate fluctuations are transformed into spectral densities in the frequency domain to build a Power Spectral Density distribution, where the Auto Power Spectral Density (APSD) and the Cross Power Spectral Density (CPSD) can be obtained. The microscopic noise occurs when neutrons are detected individually, only one neutron per bin, and they are analyzed in the time domain. The counts acquired are distributed directly into the time channels, generating a distribution as in the Rossi-α method. Other subcritical reactivity measurement techniques can be found in (Misawa and Unesaki, 2003; Shahbunder et al., 2010).

The subcritical reactivity is closely related to the kinetic model applicable to the system. Most of these measurement techniques rely on the validity of the point kinetic model (i.e. the fundamental mode approximation and a single decay mode (α-mode)), which is

* Corresponding author at: Instituto de Pesquisas Energéticas e Nucleares – IPEN/CNEN-SP, Centro de Engenharia Nuclear (CEN), Av. Prof. Lineu Prestes, 2242, 05508-000 - Cidade Universitária, São Paulo, SP, Brazil.
E-mail addresses: diogofs@msn.com (D. Feliciano dos Santos), asantos@ipen.br (A. dos Santos).

https://doi.org/10.1016/j.anucene.2020.107974
0306-4549/

not applicable in all levels of subcriticality, experimental facilities, or explain all kinds of anomalies found in subcritical measurements (Spriggs et al., 1997). Most of the anomalies are related to the kinetic behavior of reflected reactors. Furthermore, the utilization of calculated factors (Gajda et al., 2013) imposes severe restrictions and limitations on these techniques. The ICSBEP (International Criticality Safety Benchmark Evaluation Project) handbook presents the state of art regarding criticality safety benchmarks. Out of around 5000 configurations, only two of them refer to subcritical states (Bess et al., 2017). The remainder of them are critical configurations. The lack of benchmarked subcritical experiments reinforces the necessity to perform more experiments of this class that attend the requirements of the ICSBEP.

Around the world, there are approximately 245 (IAEA, 2013) research reactors out of which a good fraction are thermal reactors. This class of reactors has one thing in common, they are all small size cores reflected by some light elements such as light water, heavy water, Graphite or Beryllium. The physics involved in these compact thermal cores considers the dynamic behavior of both core and reflector, which can exhibit large differences between them. Numerous theories and models have been developed for reflected system (Avery et al., 1958; Cohn, 1962; Kobayashi, 1990; Nishina and Yamane, 1985; Shinkawa et al., 1978; Spriggs et al., 1997; Van Dam, 1996; Wasserman, 1960; Yamane et al., 1980). Several studies performed at the IPEN/MB-01 research reactor facility indicate that its core is more appropriately described by a two-region model as proposed by Spriggs (Spriggs et al., 1997). Several parameters such as β_{eff} (Kuramoto et al., 2008) and subcritical reactivities (Gonnelli and dos Santos, 2016) were measured employing the two-region model. The neutron lifetimes and several other kinetic constants in the core and reflector play an important role, since they will rule out the time response after some perturbation in these systems. Particularly, the neutron lifetimes are distinct in the core and reflector, usually, they are of the order of tenths of microseconds in the core and fractions of milliseconds in the reflector. The magnitude of these constants changes a lot depending on the physics characteristics of the core and reflector as well as they exhibit neutron energy dependency. The necessity of new physics and mathematical models for the dynamic description of these thermal systems and the experimental results to serve as benchmarks for the validation of these methods are of extreme importance. In this context, the IPEN/MB-01 research reactor can help because its core has been benchmarked in a lot of experiments (Diniz and dos Santos, 2006; dos Santos et al., 2014; 2012; 2006b;; dos Santos and Diniz, 2014; Kuramoto et al., 2008, 2007).

The main concern of this paper is to present a new experiment based on the utilization of the macroscopic reactor noise technique and a new kinetic model based on a two-group and two-region kinetic model to interpret the experiment and from that to infer some important physical quantities related to the subcritical reflected reactor systems. To accomplish the work, the specific purposes are threefold: a) to present new experimental results for the measurement of the APSD to frequencies up to 100 kHz, b) to describe the main steps of a developed two-region two-group kinetic model considering the interpretation of the measured data, and c) to analyze the kinetics of the thermal neutrons in the reactor system poisoned with 286.8 ppm of natural boron. Two subcritical cases with distinct boric acid concentrations in the moderator water tank were considered in this work. The experimental data can be useful to infer important quantities of the reactor physics field, such as subcritical reactivity, neutron lifetimes, generation times, and prompt neutron decay constants in the core and reflector regions. The focus is devoted to the zero-power research reactor and the utilization of the macroscopic neutron noise technique. The applications of the reactor noise in a zero-power reactor are extensive (dos Santos et al., 2006a; Kitamura et al., 1999; Mihalczo et al., 1990; Soule et al., 1990; Suzuki, 1966). Some recent applications of the reactor noise in research reactors were performed in Japan (Sakon et al., 2014, 2013), Sweden (Szieberth et al., 2015), and India (Kumar et al., 2016).

The experiments of high frequency performed at the IPEN/MB-01 are unique of its kind and several important aspects of the dynamic behavior of such compact reflected-core systems will become evident from the analyses of the experiments (dos Santos, 2020). Particularly, the dynamics of thermal neutrons will come out explicitly from the new model developed in this work. Kinetic parameters such as prompt neutron generation time, prompt neutron decay constants, partial reactivities all in the core and reflector are reported for the first time. A two-group and two-region kinetic model and a special numerical approach were specially developed to infer these kinetic parameters. The experimental approach developed in this work does not require any sort of correction factors. The procedure developed here is purely experimental.

2. Experimental approach

The core configuration considered a short version of the IPEN/MB-01 core in a 26 × 24 rectangular array of fuel rods. For this experiment, the outer row of fuel rods was removed in each face from the standard IPEN/MB-01 configuration (28 × 26), i.e., 104 fuel rods. Thus, almost all the reactivity excess was removed from the core. The measured reactivity was equal to (10 ± 3) pcm, with the control and the safety banks completely withdrawn. A complete description of the IPEN/MB-01 core can be found elsewhere (dos Santos et al., 2014).

The subcritical states were reached by diluting boric acid (H_3BO_3) solutions in the moderator water. The boron concentrations were (286.8 ± 10) and (578.6 ± 10) ppm (parts per million or $\mu g/g$) of natural boron for the two experiments considered here. The uncertainty of 10 ppm corresponds to the accuracy of the chemical analysis equipment. The core was driven by the ^{241}Am-Be start-up source (~1.0 Ci) of the facility placed in the reflector. In these experiments, each 1 ppm of natural boron in the water was equivalent to about 23.6 pcm of negative reactivity (dos Santos et al., 2019). This high value of specific reactivity is due to the neutronic characteristics of the IPEN/MB-01 core which has its pitch very close to the optimum pitch (maximum k_∞).

Two ^{3}He Centronic detectors were placed 167.6 mm away from the outermost fuel rods of the reactor and inside the detection channels. As shown in Fig. 1, the detection channel was at the same level as the upper surface of the bottom grid plate. Due to the high level of subcriticality, the two most sensitive detectors available in the IPEN/MB-01 facility were selected. The detectors had the thermal neutron sensitivity of 202 cps/nv (s/n 8739) and 297 cps/nv (s/n 8740). They had 100 cm of sensitive height and covered the entire active height given by the fuel rods, exceeding it by 42.5 cm approximately.

The detectors were symmetrically located in the reflector region to get the neutron counts for the IPEN/MB–01 Correlator. The counts were then summed to get better statistics in the measurements. The data acquisition and processing system employ the following procedure shown in Fig. 2.

The temperature in the fuel region was monitored by means of a set of 12 thermocouples distributed uniformly in the active region of the reactor core. The average temperature for the experiment with 286.8 ppm of natural boron was (19.82 ± 0.37) °C and that for the 578.6 ppm was (19.89 ± 0.09) °C.

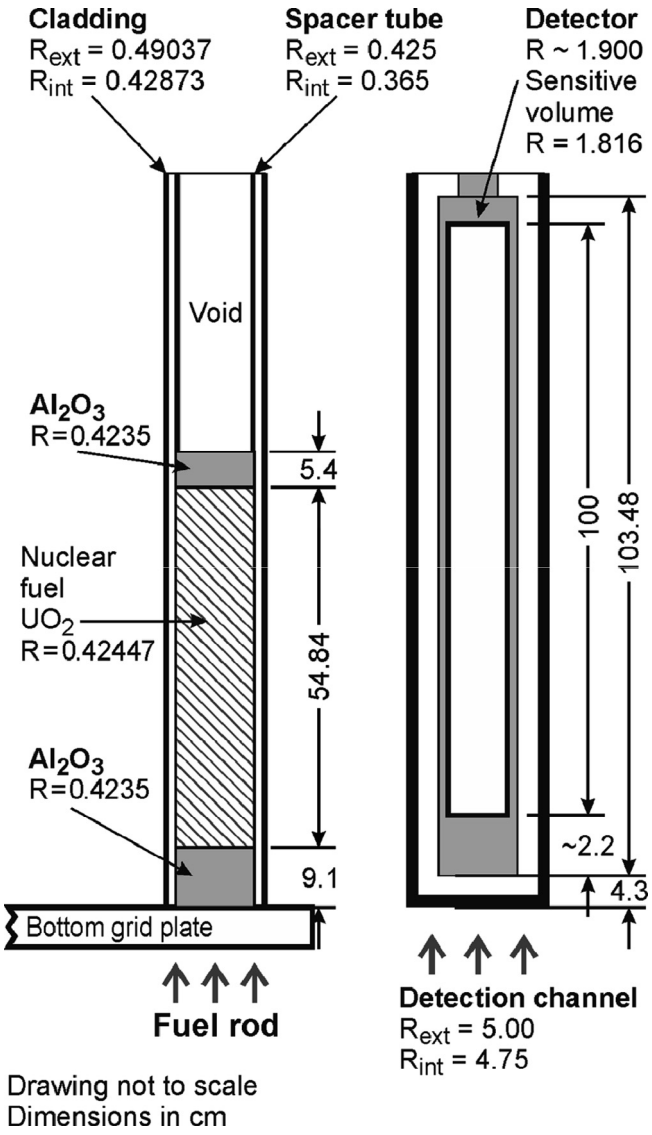

Fig. 1. Axial view of the fuel rods and the detection channel.

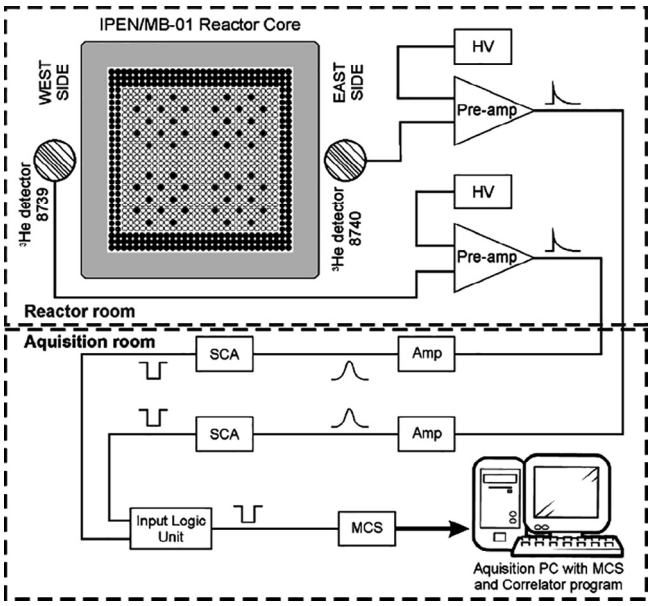

Fig. 2. The APSD measurement system.

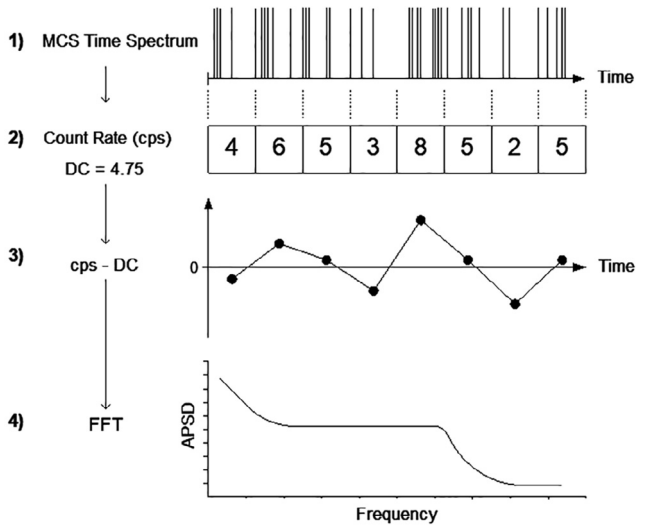

Fig. 3. Schematic View for the four processing sub-routines C/C++ to infer the spectral densities employing pulse mode detectors.

2.1. Description of the IPEN/MB-01 Correlator

According to Fig. 2 neutron pulses from the detectors were formatted and amplified by preamplifiers and amplifiers with the shaping time set to 2 μs. Subsequently, they were discriminated from the γ-radiation through the Lower Level Discriminator of the Single-Channel Analyzer (SCA). Negative logical pulses were generated in the output of the single-channel (standard NIM fast negative) with 25 ns width and −5 V of amplitude on 50 Ω impedance. Since the subcritical level was high for the two boron diluted cases considered here, the negative logic pulses were summed (merged) in a logic OR ($X = A + B$) employing an Input Logic Unit. A Multichannel Scaler (MCS) board registered the time intervals between a trigger signal and the subsequent logical pulses. The dwell time chosen for the MCS board provided the maximum frequency to be analyzed, and the number of channels gave the corresponding frequency resolution. The whole system of acquisition and signal processing is called IPEN/MB-01 Correlator, and it is a program written in LabView 5.1 (Laboratory Virtual Instrument Engineering Workbench).

The data processing is written in C/C++. Fig. 3 illustrates the data processing. The MCS transforms the pulses from the detectors into a time spectrum which represents the count rates in the detector. Once the detector count rates are obtained, the level DC (average count rate) is removed from these count rates. This is like an electronic filter, however, performed by a software. Finally, the APSD is constructed consistently to that employed in current mode by the DSA (Agilent 35670A Dynamical Signal Analyzer) (Keysight, 2017) as:

$$APSD = \frac{\sum_{i=1}^{N} FFT(CR(t))_i \cdot FFT(CR(t))_i^*}{NB}, \quad (1)$$

where FFT is the Fast Fourier Transform of $CR(t)$ (counts), $CR(t)$ is the count rate minus DC at time t (in units of cps), N is the number of averages, B is the bandwidth (Hz), and the symbol (*) represents the complex conjugate of $FFT(CR(t))$.

In this work the dwell time was set at 5 μs, the bandwidth was 4.8 Hz, the number of channels, in the time domain, was set to be 62,500 (double-sided), which resulted in a resolution of 3.2 Hz in

the frequency domain and a frequency domain from 9.6 Hz up to 100 kHz (single-sided spectrum).

The APSD unity arising from Eq. (1) is $count^2/Hz$. Experimentally, the IPEN/MB-01 Correlator is very similar to the one developed by Kitamura although there are some differences in the CPSD magnitude and its unity. The APSD derived from the IPEN/MB-01 Correlator preserves the correct units and magnitude. It has been successfully applied in the determination of the relative power in other subcritical experiments of the IPEN/MB-01 (dos Santos et al., 2013).

The APSD measurements performed by the IPEN/MB-01 Correlator considered 3,000 averages in each acquisition. Each acquisition took about 35 min to be completed. The average count rates (cps) were, respectively, (923 ± 11) cps and (198.2 ± 1.1) cps for the 286.8 and 578.6 ppm of natural boron cases. The number of acquisitions was, respectively, 12 and 163 for the 286.8 ppm and 578.6 ppm cases. The 578.6 ppm case has more acquisitions due to its high degree of subcriticality and lower detector counts. Each natural boron case has an average APSD curve calculated by the mean of the acquired individual APSDs. The uncertainty of the average APSD is obtained by the uncertainty propagation of the individual acquisitions, which has the uncertainty given by as $1/\sqrt{N}$, where N is the number of acquired count rates, named "averages".

3. Experimental results

The experimental data was least-squares fitted employing the CERN code ROOT version 6.14 running in a Linux platform. The fitting function is given by

$$\Phi(\omega) = \frac{A_7}{\omega^2 + {\omega_7}^2} + \frac{A_8}{\omega^2 + {\omega_8}^2} + \frac{A_9}{\omega^2 + {\omega_9}^2} + \frac{A_{10}}{\omega^2 + {\omega_{10}}^2} + C, \qquad (2)$$

where $\omega = 2\pi f$, being f the frequency. Each term of the Eq. (2) containing a coefficient A_j and a root ω_j is called a mode. The j index in the coefficients and roots started at seven, this is because there are no contributions from the six families of neutron precursors in the experimental data. The minimum frequency of the experimental data is above the frequency of the shortest half-life of the six families of delayed neutrons (Lamarsh, 1966). Several attempts have been made employing Eq. (2) to find the best approach to fit the experimental data (dos Santos, 2020).

Table 1 summarizes the final findings for the 286.8 ppm of natural boron for the maximum frequency that satisfy the criteria of having the reduced χ^2 as close as possible to one and the probability of the χ^2 (Prob) as close as possible to 50%. The analyses were made considering sequentially one through four modes. Particularly, one mode considers just the first term of Eq. (2) and the constant C. This is the classical APSD behavior predicted by the point kinetic theory. For this case, the maximum frequency that this model can satisfactorily fit the experimental data was 1,175 Hz, which was well below the range of measured data. The two modes that follow represent the reflector-core model as proposed firstly by Cohn (Cohn, 1962) and improved by Spriggs (Spriggs et al., 1997). The maximum frequency reached for this model was 9,650 Hz. The three-mode model also could not fit the complete set of measured data. Only, the four-mode model satisfactorily fitted the measured data. In this last case, a very important characteristic of the least-square fit was the significative reduction of the fitted parameter uncertainties.

Table 1
Maximum achievable frequency versus the number of modes.

Number of Modes	Maximum Frequency (Hz)	Reducedχ^2	Prob.(%)
1	1,175	0.9956	51.36
2	9,650	0.9982	52.39
3	27,000	0.9999	50.02
4	75,800	0.9998	50.58

The results of the least-squares fit are shown in Figs. 4 and 5 for both cases of boron dilutions. The fit for 286.8 ppm of natural boron went up to 75.8 kHz and for 578.6 ppm to 71.8 kHz. It can be noted that there are two distinct sets of fitted roots (ω_j). Two roots (ω_7, and ω_8) at lower frequencies and two roots (ω_9, and ω_{10}) at higher frequencies. It will be shown forward that the first two modes of the APSD given by Eq. (2) represent the effects of thermal neutrons and the last two models those of fast neutrons. Furthermore, the similarity of the roots ω_9, and ω_{10} values for both boron diluted cases is very noticeable. The presence of the boric acid does not change appreciably the neutron spectra in the fast neutron energy range. Finally, the absolute values of the coefficients A_7 and A_8 are anticorrelated ($A_7 \cong -A_8$) considering their uncertainty range inside 3σ. This condition is best satisfied for the 286.8 ppm case. This feature of the fitted data will be an important finding to identify the first two modes as the kinetic behavior of the thermal group. Particularly, the ratio of the A_9 coefficients of the two boron dilutions are very close to the ratio of the square of the corresponding detector counts as it was expected to be.

Figs. 4 and 5 also show the calculated reactivities in units of dollar. Here, the calculated values are from MCNP6 (Goorley et al., 2013) in conjunction with the ENDF/B-VII.0 library. The reactivity was considered relative to the case without boron in the water tank. The effective delayed neutron fraction ($\beta_{eff} = 750 \pm 5pcm$) was taken from (dos Santos et al., 2006b).

The rise shown by the APSD curves toward higher frequencies in Figs. 4 and 5 were similar to that observed in other experiments performed in the IPEN/MB-01 reactor. These experiments were performed without boron with the core configuration of the paper or the rectangular standard configuration of 28×26 fuel rod array. The subcritical reactivity was reached by inserting the control banks. The experiments employed many variations, as a variety of detectors, some different detector positions, and different associated instrumentation. These experiments were done to choose and test the detectors and the instrumentation to certify that everything was suitable for the boron poisoned reactor measurements. However, during the boron experiments, the dwell time and the number of the time channels for the two-side spectrum were altered and that behavior at higher frequencies was observed.

The boron experiments were followed afterward employing the best achievable electronic equipment setup. Particularly, the shap-

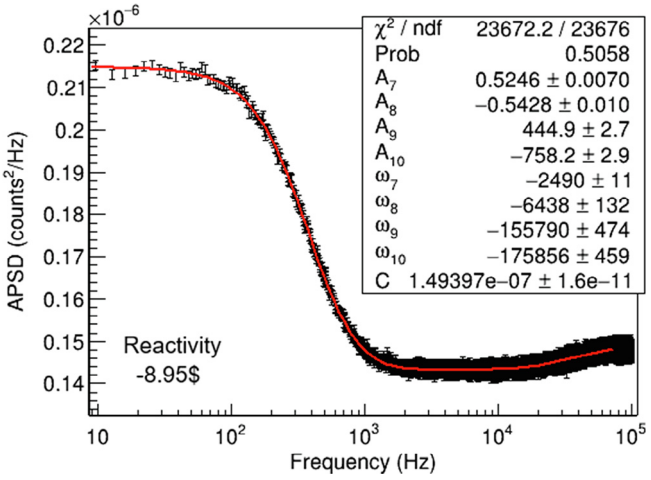

Fig. 4. APSD for the case of 286.8 ppm of natural boron.

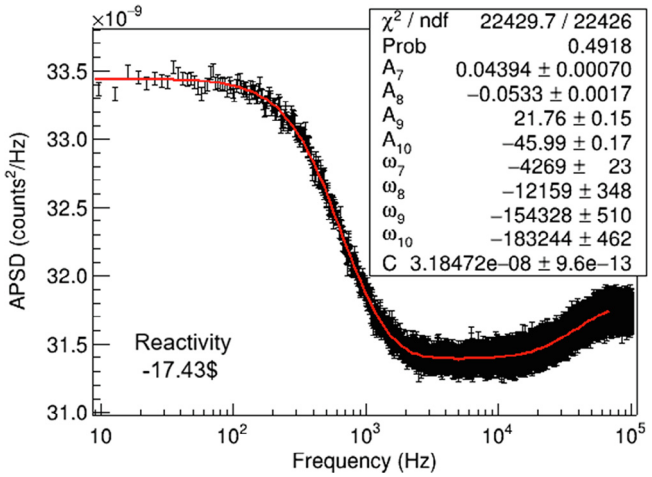

Fig. 5. APSD for the case of 578.6 ppm of natural boron.

ing time (pulse processing time) was selected to be 2 μs after several tests. This was the shortest possible shaping time that formed a spectrum of neutrons according to what was expected for the ^{3}He detectors (Knoll, 2000) used in the experiments. The ideal would be an almost zero shaping time. A longer shaping time has the quality of magnifying the fast modes at high frequencies. It was always a concern if what was being acquired at high frequencies was a physical event or something that electronic instrumentation was producing. However, the possibility is very remote of having an instrument that produced a noise that was measured in the spectrum of high frequencies and in these data the modes of the APSD function were precisely fitted. If the instrumentation produced high-frequency modes, these would have to be the same for all measurements. However, as shown in Figs. 4 and 5, the reactivity insertion with the increase of natural boron in the system changes the amplitudes of the fast modes, according to what was expected physically and being something that electronic instrumentation would not perform.

Fig. 6 shows the partial contributions of the individual modes to the measured APSD for the cases of 286.8 ppm of natural boron. The constant C in Eq. (2) was omitted in this figure and when it is considered it will make the APSD positive in all points. As can be seen, the contributions of modes 3 and 4 for frequencies below

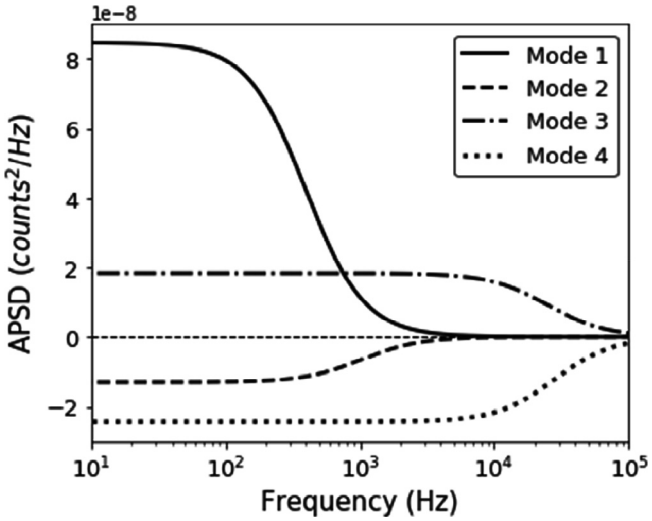

Fig. 6. Partial contributions of the individual modes to the measured APSD.

10 kHz are approximately constants. On the other hand, for frequencies higher than around 7 kHz the contributions of modes 1 and 2 go to zero. Consequently, modes 1 and 2 dominates the measured APSD at frequencies lower than 10 kHz, and conversely modes 3 and 4 dominates at higher frequencies. The frequency spectrum is, somehow, proportional to the neutron energy and the time elapsed between neutron birth and death is also implicitly linked to that. If the fission neutron does not collide with any particles on the way to the detector, then it will arrive in a very short time, resulting in a high frequency neutron. If the neutron collides near the detector and is detected, then it will also be in the high frequency spectrum. These two types of situations correspond to the fast neutrons, but of course it depends on the cross-section of ^{3}He to occur an interaction that generates electrons to transform in counts. Now as the neutron diffuses through the medium, the time from birth to detection increases, forming the low frequency spectrum, which is related to thermal neutrons. For these reasons, the first two modes dominated the lower frequency and can be identified as the thermal energy region and the remainder the fast energy region. The breakdown between thermal and fast energy range is not well defined but it is believed to be the limit of the upscattering. These findings will give rise to the development of the two-group two-region kinetic model for the interpretation of the measured APSD.

4. The Two-Group Two-Region neutron kinetic Model

The available theoretical models (Avery et al., 1958; Cohn, 1962; Kobayashi, 1990; Nishina and Yamane, 1985; Shinkawa et al., 1978; Spriggs et al., 1997; Van Dam, 1996; Wasserman, 1960; Yamane et al., 1980) do not explain all the findings the experiment revealed. The developed model shown in this section is a tentative to explain the experiment and to infer some important properties of the physics of the IPEN/MB-01 reactor.

The experiments clearly show that there are two distinct frequency ranges. It suggests that the appropriate model to describe the high-frequency experiment performed in the IPEN/MB-01 reactor is a two-group and two-region kinetic model. Due to its complexity and its lengthy development, only the main steps of the development are shown here. A complete description of this kinetic model can be found in (dos Santos, 2020).

Consider that a reactor in a critical state is suddenly perturbed and the physical constants of the transport equation are changed by a specific amount, e.g., $\sigma = \sigma_0 + \Delta\sigma$, and a neutron source is suddenly inserted into the system. The temperature feedback is neglected for this transient. Consider further the traditional way to get the time behavior of the transient, as in ref. (Bell and Glasstone, 1970), and a two-region problem consisted of a core and a reflector region, as shown in Fig. 7.

Here the notation is the same as that in (Bell and Glasstone, 1970). The fundamental equations governing this transient is the neutron transport equation given by:

$$\begin{aligned}\frac{1}{v(E)}\frac{\partial\Phi(\boldsymbol{r},\Omega,E,t)}{\partial t} &+ \Omega\cdot\nabla\Phi(\boldsymbol{r},\Omega,E,t) + \sigma(\boldsymbol{r},E,t)\Phi(\boldsymbol{r},\Omega,E,t)\\ &= \iint\sum_{x\neq f}\sigma_x\left(\boldsymbol{r},E',t\right)f_x\left(\boldsymbol{r};\Omega',E'\rightarrow\Omega,\mathrm{E},t\right)\Phi\left(\boldsymbol{r},\Omega',E',t\right)d\Omega'dE'\\ &+ \iint\chi_p(E)\left[1-\beta\left(E'\right)\right]\nu\left(\boldsymbol{r},E'\right)\sigma_f\left(\boldsymbol{r},E',t\right)\Phi\left(\boldsymbol{r},\Omega',E',t\right)d\Omega'dE'\\ &+ \sum_{j=1}^{6}\lambda_j C_j(\boldsymbol{r},t)\chi_j(E) + Q(\boldsymbol{r},\Omega,E,t),\end{aligned} \tag{3}$$

and the delayed neutron precursor equation given by:

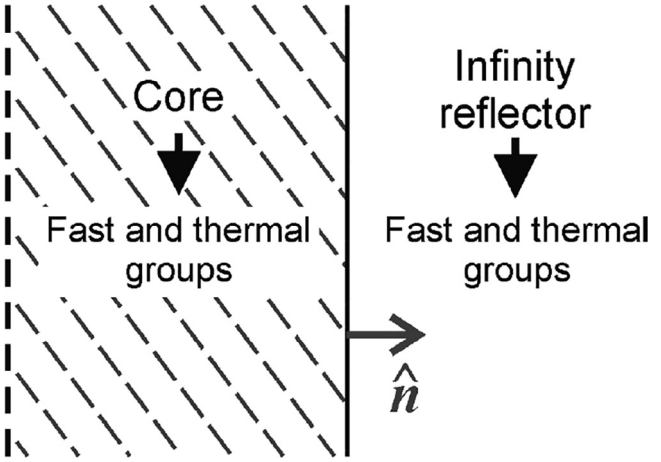

Fig. 7. The two-region model adopted to describe the experiment.

$$\frac{\partial C_j(\boldsymbol{r},t)}{\partial t}+\lambda_j C_j(\boldsymbol{r},t)=\iint \beta_j\left(E^{'}\right)\nu\left(\boldsymbol{r},E^{'}\right)\sigma_f\left(\boldsymbol{r},E^{'},t\right)\Phi\left(\boldsymbol{r},\Omega^{'},E^{'},t\right)d\Omega^{'}dE^{'}. \tag{4}$$

To derive the two-group two-regions kinetic model consider the neutron transport adjoint equation at the critical state as:

$$\begin{aligned}-\Omega\cdot\nabla\Phi_0^{\dagger}(r,\Omega,E)+\sigma_0(r,E)\Phi_0^{\dagger}(r,\Omega,E)\\ =\iint\sum_{x\neq f}\sigma_{x0}(\mathrm{r},\mathrm{E}')\mathrm{f}_{x0}(\mathrm{r};\Omega,\mathrm{E}\rightarrow\Omega',\mathrm{E}')\Phi_0^{\dagger}(\mathrm{r},\Omega',\mathrm{E}')\mathrm{d}\Omega'\mathrm{dE}'\\ +\nu(\mathrm{r},\mathrm{E})\sigma_{f0}(\mathrm{r},\mathrm{E})\iint\tilde{\chi}(\mathrm{E},\mathrm{E}')\Phi_0^{\dagger}(\mathrm{r},\Omega',\mathrm{E}')\mathrm{d}\Omega'\mathrm{dE}',\end{aligned} \tag{5}$$

where:

$$\tilde{\chi}(E,E')=[1-\beta(E)]\tilde{\chi}_p(E')+\sum_{j=1}^{6}\beta_j(E)\tilde{\chi}_j(E') \tag{6}$$

The kinetic equations will be derived in a two-group model following the traditional way as:

a) Initially, the direct and the adjoint transport equations are written in the core and reflector regions.
b) In each one of these regions, the adjoint transport equation is multiplied by the corresponding direct neutron flux and the direct transport equation by the adjoint flux.
c) The resultant equations for each region are then subtracted,
d) The neutron flux is factored for group g and region x in an amplitude and a shape factor as:

$$\Phi_x^g(\boldsymbol{r},\Omega,E,t)=N_x^g(t)\psi_x^g(\boldsymbol{r},\Omega,E,t), \tag{7}$$

where $\Phi_x^g(\boldsymbol{r},\Omega,E,t)$, $N_x^g(t)$ and $\psi_x^g(\boldsymbol{r},\Omega,E,t)$ are respectively the neutron flux, the amplitude and the shape factors for group g and region x. The shape factor depends on the energy group (thermal and fast) and the reactor region (core or reflector). The IPEN/MB-01 is a zero-power reactor, thus the shape factor can be considered constant over time for the subcritical experiment considered here.

e) The set of equations is integrated over the phase space $(\boldsymbol{r},\Omega,E)$, where $\boldsymbol{r}$ represents the neutron flux position, Ω the neutron direction, and E the neutron energy. Here the space integral is performed in the core and reflector regions individually and the integral in the neutron energy is performed in the thermal and fast groups, also individually. The interval of the thermal group is between 0 and E_T, where E_T is the maximum thermal energy, and that of the fast group between E_T and infinite.
f) The final set of equations derived consider specifically the case of poisoning the moderator water, both in the core and reflector, due to the insertion of boric acid in the reactor tank water. This specific case of perturbation possesses the special characteristic of inducing reactivity predominantly in the thermal neutron energy range, where the boron absorption cross-section is more effective. The reactivity effect in the fast neutron energy range will be considered negligible and it will not be in the coming development.

The final set of linear coupled differential equations for the amplitude factor in each region (core and reflector) and each neutron energy group (thermal and fast) is:

$$\frac{dN_c^F}{dt}=-\frac{\beta_{eff}^{FF}}{\Lambda_c^F}N_c^F-\frac{j_{c\rightarrow r}^F}{\Lambda_c^F}N_c^F+\frac{j_{r\rightarrow c}^F}{\Lambda_c^F}N_r^F-\frac{X_{1c}^{FT}}{\Lambda_c^F}N_c^F+\frac{F_{1p}^{TF}}{\Lambda_c^F}N_c^T+\sum_{j=1}^{6}\lambda_j c_j^F+S_c^F; \tag{8}$$

$$\frac{dN_r^F}{dt}=\frac{j_{c\rightarrow r}^F}{\Lambda_r^F}N_c^F-\frac{j_{r\rightarrow c}^F}{\Lambda_r^F}N_r^F-\frac{X_{1r}^{FT}}{\Lambda_r^F}N_r^F+S_r^F; \tag{9}$$

$$\frac{dc_j^F}{dt}=\frac{\beta_j^{FF}}{\Lambda_c^F}N_c^F+\frac{\beta_j^{TF}}{\Lambda_c^F}N_c^T-\lambda_j c_j^F; \tag{10}$$

$$\frac{dN_c^T}{dt}=\frac{\rho_c^{TT}-\beta_{eff}^{TF}}{\Lambda_c^T}N_c^T-\frac{j_{c\rightarrow r}^T}{\Lambda_c^T}N_c^T+\frac{j_{r\rightarrow c}^T}{\Lambda_c^T}N_r^T+\frac{X_{1c}^{FT}}{\Lambda_c^T}N_c^F-\frac{F_{1p}^{TF}}{\Lambda_c^T}N_c^T; \tag{11}$$

$$\frac{dN_r^T}{dt}=\frac{\rho_r^{TT}}{\Lambda_r^T}N_r^T+\frac{j_{c\rightarrow r}^T}{\Lambda_r^T}N_c^T-\frac{j_{r\rightarrow c}^T}{\Lambda_r^T}N_r^T+\frac{X_{1r}^{FT}}{\Lambda_r^T}N_r^F; \tag{12}$$

where the superscripts T and F refer respectively to the thermal and fast neutron energy group, the subscripts c and r refer respectively to the core and reflector region, c_j^F is the adjoint weighted precursor density for family j, λ_j is the precursor decay constant for family j, β is the effective delayed neutron fraction either total or in the family j, ρ is the reactivity, $j_{c\rightarrow r}$ is the neutron current from the core to the reflector and $j_{r\rightarrow c}$ is the neutron current in the opposite direction. The superscripts FF, FT, TF, and TT represents that a double integral is being performed inside the triple integral. X^{FT} represents the transfer of fast neutrons to the thermal group, F_{1p}^{TF} represents the production of prompt fast neutrons due to thermal fissions. Λ is the prompt neutron generation time. The quantities involved in Eqs. (8) through (12) are defined as follow:

$$\Lambda_c^F\equiv\frac{1}{G_c}\int_{E_T}^{\infty}\int_{4\pi}\int_c\frac{1}{\nu}\Phi_0^{\dagger}\psi\ dVd\boldsymbol{\Omega}dE; \tag{13}$$

$$c_j^F\equiv\frac{1}{\Lambda_c G_c}\int_{E_T}^{\infty}\int_{4\pi}\int_c\Phi_0^{\dagger}\tilde{\chi}_j C_j\ dVd\boldsymbol{\Omega}dE; \tag{14}$$

$$S_c^F\equiv\frac{1}{\Lambda_c^F G_c}\int_{E_T}^{\infty}\int_{4\pi}\int_c\Phi_0^{\dagger}Q\ dVd\boldsymbol{\Omega}dE; \tag{15}$$

$$j_{c\rightarrow r}^F\equiv\frac{1}{G_c}\left|\int_{E_T}^{\infty}\int_{\hat{\boldsymbol{n}}\cdot\Omega>0}\int_c\hat{\boldsymbol{n}}\cdot\boldsymbol{\Omega}\Phi_0^{\dagger}\psi\ dAd\boldsymbol{\Omega}dE\right|; \tag{16}$$

$$j^{F}_{r\to c} \equiv \frac{1}{G_c}\left|\int_{E_T}^{\infty}\int_{\hat{\mathbf{n}}\cdot\mathbf{\Omega}<0}\int_c \hat{\mathbf{n}}\cdot\mathbf{\Omega}\Phi^{\dagger}_0\psi\ dAd\mathbf{\Omega}dE\right|; \tag{17}$$

$$X^{FT}_{1c} \equiv \frac{1}{G_c}\int_0^{E_T}\int_{4\pi}\int_c \Phi^{\dagger}_0\left(\int_{E_T}^{\infty}\int_{4\pi}\sum_{x\neq f}\sigma'_{x0}f_{x0}\psi' d\mathbf{\Omega}'dE'\right)dVd\mathbf{\Omega}dE; \tag{18}$$

$$F^{TF}_{1p} \equiv \frac{1}{G_c}\int_{E_T}^{\infty}\int_{4\pi} \times\int_c \Phi^{\dagger}_0\left(\int_0^{E_T}\int_{4\pi}(1-\beta')\tilde{\chi}_p\nu'\sigma'_{f0}\psi' d\mathbf{\Omega}'dE'\right)dVd\mathbf{\Omega}dE; \tag{19}$$

$$\beta^{FF}_{eff} \equiv \frac{1}{G_c}\int_{E_T}^{\infty}\int_{4\pi} \times\int_c \Phi^{\dagger}_0\left(\int_{E_T}^{\infty}\int_{4\pi}\sum_{j=1}^{6}\tilde{\chi}_j\beta'_j\nu'\sigma'_f\psi' d\mathbf{\Omega}'dE'\right)dVd\mathbf{\Omega}dE; \tag{20}$$

$$X^{FT}_{1r} \equiv \frac{1}{G_c}\int_0^{E_T}\int_{4\pi}\int_r \Phi^{\dagger}_0\left(\int_{E_T}^{\infty}\int_{4\pi}\sum_{x\neq f}\sigma'_{x0}f_{x0}\psi' d\mathbf{\Omega}'dE'\right)dVd\mathbf{\Omega}dE; \tag{21}$$

$$\Lambda^{F}_r \equiv \frac{1}{G_c}\int_{E_T}^{\infty}\int_{4\pi}\int_r \frac{1}{\nu}\Phi^{\dagger}_0\psi\ dVd\mathbf{\Omega}dE; \tag{22}$$

$$S^{F}_r \equiv \frac{1}{\Lambda^{F}_r G_c}\int_{E_T}^{\infty}\int_{4\pi}\int_r \Phi^{\dagger}_0 Q\ dVd\mathbf{\Omega}dE; \tag{23}$$

$$\beta^{TF}_{eff} \equiv \frac{1}{G_c}\int_{E_T}^{\infty}\int_{4\pi} \times\int_c \Phi^{\dagger}_0\left(\int_0^{E_T}\int_{4\pi}\sum_{j=1}^{6}\tilde{\chi}_j\beta'_j\nu'\sigma'_f\psi' d\mathbf{\Omega}'dE'\right)dVd\mathbf{\Omega}dE; \tag{24}$$

$$\rho^{TT}_c \cong -\frac{1}{G_c}\int_0^{E_T}\int_{4\pi}\int_c \Phi^{\dagger}_0\Delta\sigma\psi\ dVd\mathbf{\Omega}dE; \tag{25}$$

$$j^{T}_{c\to r} \equiv \frac{1}{G_c}\left|\int_0^{E_T}\int_{\hat{\mathbf{n}}\cdot\mathbf{\Omega}>0}\int_c \hat{\mathbf{n}}\cdot\mathbf{\Omega}\Phi^{\dagger}_0\psi\ dAd\mathbf{\Omega}dE\right|; \tag{26}$$

$$j^{T}_{r\to c} \equiv \frac{1}{G_c}\left|\int_0^{E_T}\int_{\hat{\mathbf{n}}\cdot\mathbf{\Omega}<0}\int_c \hat{\mathbf{n}}\cdot\mathbf{\Omega}\Phi^{\dagger}_0\psi\ dAd\mathbf{\Omega}dE\right|; \tag{27}$$

$$\Lambda^{T}_c \equiv \frac{1}{G_c}\int_0^{E_T}\int_{4\pi}\int_c \frac{1}{\nu}\Phi^{\dagger}_0\psi\ dVd\mathbf{\Omega}dE; \tag{28}$$

$$\rho^{TT}_r \cong -\frac{1}{G_c}\int_0^{E_T}\int_{4\pi}\int_r \Phi^{\dagger}_0\Delta\sigma\psi\ dVd\mathbf{\Omega}dE; \tag{29}$$

$$\Lambda^{T}_r \equiv \frac{1}{G_c}\int_0^{E_T}\int_{4\pi}\int_r \frac{1}{\nu}\Phi^{\dagger}_0\psi\ dVd\mathbf{\Omega}dE; \tag{30}$$

and

$$G_c \equiv \int_0^{\infty}\int_{4\pi}\int_c \Phi^{\dagger}_0\left(\int_0^{\infty}\int_{4\pi}\tilde{\chi}\ \nu'\sigma'_f\psi' d\mathbf{\Omega}'dE'\right)dVd\mathbf{\Omega}dE\ . \tag{31}$$

The single quotes (′) in the quantities of Eqs. (13) through (31) indicates the incident neutron direction Ω' and energy E' and those without single quotes indicate the quantities are relative to the outgoing neutron direction Ω and energy E.

It must be noted in the set of Eqs. (8) through (12) that there is no explicit source in the thermal neutron energy group equations. All sources involved in the experiment generate fast neutrons. The reactivity in the thermal group has been split into a core (ρ^{TT}_c) and a reflector (ρ^{TT}_r) contributions. The total reactivity induced by the addition of the boric acid in the moderator water is a sum of these two contributions. The effective delayed neutron fraction was also split into a fast (β^{FF}_{eff}) and a thermal (β^{FT}_{eff}) parts. The total effective delayed neutron fraction is a sum of these two parts.

4.1. Reflected core equations for the thermal group

The experiment results showed that the coupling between fast and thermal modes is weak and it is a good approximation to consider the set of Eqs. (8) through (12) uncoupled. This can be accomplished neglecting the coupling parameters X^{FT}_{1c}, X^{FT}_{1r}, and F^{TF}_{1p} in Eqs. (8), (9), (11), and (12). Due to the extensive work to be performed both analytically and numerically only the thermal group will be analyzed and applied in the experiment of 286.6 ppm of natural boron in this work.

Considering these approximations, the set of thermal neutron amplitude equations in the core and reflector regions is given by:

$$\frac{dN^{T}_c}{dt} = \frac{\rho^{TT}_c - \beta^{TF}_{eff}}{\Lambda^{T}_c}N^{T}_c - \frac{j^{T}_{c\to r}}{\Lambda^{T}_c}N^{T}_c + \frac{j^{T}_{r\to c}}{\Lambda^{T}_c}N^{T}_r \tag{32}$$

and

$$\frac{dN^{T}_r}{dt} = \frac{\rho^{TT}_r}{\Lambda^{T}_r}N^{T}_r + \frac{j^{T}_{c\to r}}{\Lambda^{T}_r}N^{T}_c - \frac{j^{T}_{r\to c}}{\Lambda^{T}_r}N^{T}_r. \tag{33}$$

Following the traditional way of solving the kinetic equations, first, it is considered a Laplace transform of Eqs. (32) and (33). The result for the core region is:

$$\mathbf{L^{T}_c}(s) = \frac{N^{T}_{c0}\Lambda^{T}_c + \frac{j^{T}_{r\to c}\Lambda^{T}_r}{s\Lambda^{T}_r - \rho^{TT}_r + j^{T}_{r\to c}}N^{T}_{r0}}{s\Lambda^{T}_c + \frac{(s\Lambda^{T}_r - \rho^{TT}_r)j^{T}_{c\to r}}{s\Lambda^{T}_r - \rho^{TT}_r + j^{T}_{r\to c}} + \beta^{TF}_{eff} - \rho^{TT}_c}. \tag{34}$$

where $\mathbf{L^{T}_c}(s)$ is the Laplace transform of $N^{T}_c(t)$, N^{T}_{c0} and N^{T}_{r0} are the initial conditions for the core and reflector neutron amplitude, respectively.

The core time-dependent equation associated to the thermal amplitude factor is the inverse Laplace transform of Eq. (34) and it is given by:

$$N^{T}_c(t) = \sum_j \frac{N^{T}_j}{\omega_j}e^{\omega_j t}, \tag{35}$$

where j is either 7 or 8 to be compatible to the experimental results, $s = \omega_j$ are the poles of Eq. (34), and

$$N_j^T = \frac{N_{c0}^T\left(\alpha_c\Lambda_c^T - \frac{\beta_r}{\alpha_r}\right)}{\Lambda_c^T + \frac{\beta_r}{(\omega_j-\alpha_r)^2}}, \tag{36}$$

where

$$\alpha_c = \frac{\rho_c^{TT} - \beta_{eff}^{TF} - j_{c\to r}^T}{\Lambda_c^T}, \tag{37}$$

$$\alpha_r = \frac{\rho_r^{TT} - j_{r\to c}^T}{\Lambda_r^T}, \tag{38}$$

and

$$\beta_r = \frac{j_{c\to r}^T j_{r\to c}^T}{\Lambda_r^T}. \tag{39}$$

The poles of Eq. (34) can be found by setting its denominator equals to zero. This gives rise to the Inhour equation for the two-group two-region thermal kinetic model as:

$$\rho_c^{TT} = \omega_j\Lambda_c^T + \frac{\left(\omega_j\Lambda_r^T - \rho_r^{TT}\right)j_{c\to r}^T}{\omega_j\Lambda_r^T - \rho_r^{TT} + j_{r\to c}^T} + \beta_{eff}^{TF}. \tag{40}$$

Eq. (40) for a given thermal reactivity ρ_c^{TT} and a set of parameters Λ_c^T, Λ_r^T ρ_r^{TT} $j_{c\to r}^T$, and $j_{r\to c}^T$ is a quadratic equation and possesses two roots, which is designated as ω_7 and ω_8 for the consistence to the experimental thermal roots (Fig. 4).

In the experiments, the detectors were placed in the reflector and the APSD measurements were acquired in that region with the consideration of the events caused in the reactor core. Thus, the major concern here is to obtain the time-dependent equation associated with the thermal amplitude factor in the reflector region. This is obtained by substituting Eq. (35) into Eq. (33) and solving the resulting equation. The final solution is written as:

$$N_r^T(t) = \left[N_{r0}^T - \frac{j_{c\to r}^T}{\Lambda_r^T}\sum_j \frac{N_j^T}{\omega_j(\omega_j-\alpha_r)}\right]e^{\alpha_r t} + \frac{j_{c\to r}^T}{\Lambda_r^T}\sum_j \frac{N_j^T}{\omega_j(\omega_j-\alpha_r)}e^{\omega_j t}. \tag{41}$$

The APSD in the reflector region is the Fourier transform of Eq. (41) and it is found as:

$$N_r^T(\omega) = \frac{-2\alpha_r\left[N_{r0}^T - \frac{j_{c\to r}^T}{\Lambda_r^T}\sum_j \frac{N_j^T}{\omega_j(\omega_j-\alpha_r)}\right]}{\alpha_r^2+\omega^2} + \sum_j \frac{A_j}{\omega_j^2+\omega^2}, \tag{42}$$

where

$$A_j = -2\frac{j_{c\to r}^T}{\Lambda_r^T}\frac{N_j^T}{(\omega_j-\alpha_r)}. \tag{43}$$

It can be demonstrated that $N_r^T(\omega)$ possesses the following property:

$$-2\alpha_r\left[N_{r0}^T - \frac{j_{c\to r}^T}{\Lambda_r^T}\sum_j \frac{N_j^T}{\omega_j(\omega_j-\alpha_r)}\right] = 0 \tag{44}$$

and consequently,

$$N_r^T(\omega) = \sum_{j=7}^{8}\frac{A_j}{\omega_j^2+\omega^2}. \tag{45}$$

4.2. Additional equations arising from the thermal neutron kinetic model

The purpose of this subsection is to show a new form of some equations from the thermal neutron kinetic model. Whenever is possible, the equations will be written as a function of the basic parameters α_c, α_r, β_r, Λ_c^T, Λ_r^T,ρ_c^{TT}, ρ_r^{TT}, $j_{r\to c}^T$, and $j_{c\to r}^T$ as arising from the two-group two-region kinetic model derived previously. These equations are properties of the two-region two-group model and they will be used in the numerical approach developed in this work to infer the basic thermal parameters which are of interest for the reactor physics area.

The Inhour equation given by Eq. (40) can be written in a more convenient form employing Eqs. (37) to (39) as:

$$\rho_c^{TT} = \omega_j\Lambda_c^T + j_{c\to r}^T - \frac{\beta_r}{\omega_j-\alpha_r} + \beta_{eff}^{TF}. \tag{46}$$

A similar equation for the thermal reflector reactivity (ρ_r^{TT}) can be found employing Eq. (40) as:

$$\rho_r^{TT} = \omega_j\Lambda_r^T + j_{r\to c}^T - \frac{\Lambda_r^T}{\Lambda_c^T}\left(\frac{\beta_r}{\omega_j-\alpha_c}\right). \tag{47}$$

Eq. (40) gives raise to another equation for thermal reflector reactivity given by

$$\rho_r^{TT} = \omega_j\Lambda_r^T + \frac{\left[(\omega_j-\alpha_c)\Lambda_c^T - j_{c\to r}^T\right](\omega_j-\alpha_r)\Lambda_r^T}{j_{c\to r}^T}. \tag{48}$$

The addition of boric acid into the reactor tank water inserted a negligible reactivity in the fast group, so the total reactivity is basically the thermal one; $\rho \cong \rho^{TT}$. Accordingly, the total reactivity (ρ) is defined as:

$$\rho = \rho_c^{TT} + \rho_r^{TT}. \tag{49}$$

Consequently,ρ can be found from the sum of Eqs. (46) and (47) as

$$\rho = \omega_j\Lambda^T + j_{c\to r}^T + j_{r\to c}^T - \left[\frac{1}{\omega_j-\alpha_r} + \frac{\Lambda_r^T}{\Lambda_c^T}\left(\frac{1}{\omega_j-\alpha_c}\right)\right]\beta_r + \beta_{eff}^{TF}, \tag{50}$$

where Λ^T is the prompt neutron generation time in the thermal group and it is given by:

$$\Lambda^T = \Lambda_c^T + \Lambda_r^T. \tag{51}$$

Very useful equation for Λ_c^T can be obtained by making $\rho_c^{TT}(\omega_7) = \rho_c^{TT}(\omega_8)$ in Eq. (46):

$$\Lambda_c^T = -\frac{\beta_r}{(\omega_7-\alpha_r)(\omega_8-\alpha_r)}. \tag{52}$$

Eq. (46) can be rewritten in a more convenient form by employing Eq. (37) as:

$$\omega_j^2 - (\alpha_c+\alpha_r)\omega_j + \alpha_c\alpha_r - \frac{\beta_r}{\Lambda_c^T} = 0, \tag{53}$$

which possesses the following properties:

$$\omega_7 + \omega_8 = \alpha_c + \alpha_r \tag{54}$$

and

$$\omega_7\omega_8 = \alpha_c\alpha_r - \frac{\beta_r}{\Lambda_c^T}. \tag{55}$$

The roots of Eq. (53) can be found employing the Bhaskara (Stillwell, 2004) formula as:

$$\omega_j = \frac{\alpha_c+\alpha_r}{2} \pm \sqrt{\left(\frac{\alpha_c+\alpha_r}{2}\right)^2 - \alpha_c\alpha_r + \frac{\beta_r}{\Lambda_c^T}}, \tag{56}$$

where the positive signal corresponds to ω_7 and the negative to ω_8.

Another useful equation can be found by combining Eqs. (37), (38) and (40). In this case the final equation is:

$$\omega_j^2 - (\alpha_c + \alpha_r)\omega_j + \alpha_c\alpha_r + \frac{j_{c\to r}^T}{\Lambda_c^T}\left(\alpha_r - \frac{\rho_r^{TT}}{\Lambda_r^T}\right) = 0, \tag{57}$$

whose solution is:

$$\omega_j = \frac{\alpha_c + \alpha_r}{2} \pm \sqrt{\left(\frac{\alpha_c + \alpha_r}{2}\right)^2 - \alpha_c\alpha_r - \frac{j_{c\to r}^T}{\Lambda_c^T}\left(\alpha_r - \frac{\rho_r^{TT}}{\Lambda_r^T}\right)}. \tag{58}$$

Again, the positive signal corresponds to ω_7 and the negative to ω_8.

A third version for the ω_j equation can be found substituting Eqs. (37) and (38) in Eq. (58):

$$\omega_j = \frac{\alpha_c\Lambda_r^T + \rho_r^{TT} - j_{r\to c}^T}{2\Lambda_r^T} \pm \sqrt{\left(\frac{\alpha_c\Lambda_r^T + \rho_r^{TT} - j_{r\to c}^T}{2\Lambda_r^T}\right)^2 - \alpha_r\left(\frac{\rho_c^{TT} - \beta_{eff}^{TF} - j_{c\to r}^T}{\Lambda_c^T}\right) - \frac{j_{c\to r}^T}{\Lambda_c^T}\left(\alpha_r - \frac{\rho_r^{TT}}{\Lambda_r^T}\right)}. \tag{59}$$

Eq. (48) gives the following relationship for α_r:

$$\alpha_r = \omega_j + \frac{\left(\omega_j - \frac{\rho_r^{TT}}{\Lambda_r^T}\right)j_{c\to r}^T}{(\omega_j - \alpha_c)\Lambda_c^T - j_{c\to r}^T}. \tag{60}$$

Eq. (44) gives the following relationship for α_c:

$$\alpha_c = \frac{\beta_r}{\alpha_r\Lambda_c^T} - \frac{1}{\frac{\alpha_r\Lambda_c^T}{\Lambda_c^T\omega_7(\omega_7-\alpha_r)+\frac{\beta_r\omega_7}{\omega_7-\alpha_r}} + \frac{\alpha_r\Lambda_c^T}{\Lambda_c^T\omega_8(\omega_8-\alpha_r)+\frac{\beta_r\omega_8}{\omega_8-\alpha_r}}}. \tag{61}$$

Considering now the APSD coefficients, it can be further demonstrated with the use of Eq. (43) that the coefficient A_7 is equal to $-A_8$. This is the main reason to associate the first two modes of the fitted measured APSD to the thermal group. The ratio $-A_7/A_8$ can be obtained from Eq. (43) and it is indicated by A. This ratio will be used in the coming section and it is given by:

$$A = -\frac{\Lambda_c^T(\omega_8 - \alpha_r) + \frac{\beta_r}{(\omega_8-\alpha_r)}}{\Lambda_c^T(\omega_7 - \alpha_r) + \frac{\beta_r}{(\omega_7-\alpha_r)}}. \tag{62}$$

4.3. Thermal neutron lifetime

The neutron lifetime is the average time from the emission of a prompt neutron in fission to the removal of the neutron by some physical process such as escape or absorption (Spriggs and Busch, 1997; X-5 Monte Carlo Team, 2008). The definition of the neutron lifetime is

$$\tau = \frac{\left\langle \frac{1}{\nu}\Phi_0^\dagger, \psi \right\rangle}{\left\langle \Phi_0^\dagger, (\nabla\cdot\boldsymbol{J} + \sigma_a\psi) \right\rangle}, \tag{63}$$

where the bracket represents the following mathematical relationship:

$$\langle A, B\rangle = \int ABdVd\Omega dE, \tag{64}$$

being the product of the functions A and B dependent on $(\boldsymbol{r}, \Omega, E)$.

Eq. (63) can be written in a more convenient form by multiplying and dividing this equation by the fission term $G_c(t)$ from Eq. (31), resulting in:

$$\tau = \frac{\left\langle \frac{1}{\nu}\Phi_0^\dagger, \psi \right\rangle}{\left\langle \Phi_{0c}^\dagger, \int\int \chi^{\sim'}\nu'\sigma_f'\psi_c' d\boldsymbol{\Omega}' dE' \right\rangle} \frac{\left\langle \Phi_{0c}^\dagger, \int\int \tilde{\chi}'\nu'\sigma_f'\psi_c' d\boldsymbol{\Omega}' dE' \right\rangle}{\left\langle \Phi_0^\dagger, (\nabla\cdot\boldsymbol{J} + \sigma_a\psi) \right\rangle}, \tag{65}$$

where the first term in the right-hand side is the prompt neutron generation time (Λ) and the second one is k_{eff}. Consequently:

$$\tau = \Lambda k_{eff}. \tag{66}$$

In a thermal reactor such as IPEN/MB-01, the fast neutrons are promptly thermalized; therefore the neutron lifetime is essentially the thermal neutron lifetime ($\tau \cong \tau^T$) (Lamarsh, 1966) and the thermal neutrons lifetime can be written as:

$$\tau^T = \Lambda^T k_{eff}, \tag{67}$$

where the effective multiplication factor k_{eff} is given by:

$$k_{eff} = \frac{1}{1-\rho}, \tag{68}$$

and ρ is given by Eq. (49). Eq. (67) shows that for a subcritical system the thermal lifetime must be lower than the thermal neutron generation time.

Another way to get the lifetime is considering the amplitude of the neutron flux as a function of time which is given by:

$$N^T = N_0^T\left(A_7 e^{\omega_7 t} + A_8 e^{\omega_8 t}\right), \tag{69}$$

where N_0^T represents the initial condition for the thermal neutron flux amplitude (Lamarsh, 1966). Because the root ω_8 is much lower than the root ω_7, as the time increases, the exponential function for ω_8 decay more rapidly than that for ω_7. Consequently, the amplitude of the thermal neutron flux can be written approximately as:

$$N^T \cong N_0^T A_7 e^{\omega_7 t}. \tag{70}$$

The amplitude of the thermal neutron flux is also given by (X-5 Monte Carlo Team, 2008):

$$N^T = N_0^T A_7 e^{\left(k_{eff}-1\right)t/\tau^T}. \tag{71}$$

Making Eq. (70) equal to Eq. (71), the thermal neutron lifetime can be written as:

$$\tau^T = \frac{k_{eff} - 1}{\omega_7}. \tag{72}$$

5. Inference of the basic parameters of the Two-group Two-Region kinetic model

The quantities measured in the experimental approach are the four roots ω_j and the four coefficients A_j. The thermal neutron energy region model developed in Section 4 considers only part of these measured data. Namely, they are ω_7, ω_8, A_7, and A_8. The unknowns in the thermal neutron energy region are α_c, α_r, β_r, Λ_c^T, Λ_r^T,ρ_c^{TT}, ρ_r^{TT}, $j_{r\to c}^T$, and $j_{c\to r}^T$. The number of unknowns is higher than the number of equations which makes impossible an analytic solution. The least-squares technique also showed a severe degeneracy among the variables making this technique useless for solving the thermal constant unknowns. Consequently, this work developed a special approach to cope with this task.

The approach of determining the quantities of the experiment with 286.8 ppm of natural boron was divided into two parts using numerical calculations with iterative algorithms. Initially, the determination of α_c, α_r, β_r, and Λ_c^T was obtained and subsequently the determination of Λ_r^T,ρ_c^{TT}, ρ_r^{TT}, $j_{r\to c}^T$, and $j_{c\to r}^T$ was carried out. The only hypothesis made was to assume that the thermal effective delayed neutron fraction (β_{eff}^{TF}) was independent of the subcritical reactivity level. This parameter was estimated to be 90% of the total β_{eff}; i.e. the sum of the thermal and fast groups. The value of the β_{eff}, (750 ± 5) pcm, utilized in this work was taken from a previous benchmark available at the NEA IRPhE handbook (dos Santos et al., 2006b). This benchmark describes the evaluation of

$\beta_{eff}$of the IPEN/MB-01 reactor in the 28 × 26 fuel rod array configuration without boron in the moderator water.

5.1. The inference of α_c, α_r, β_r, and Λ_c^T

Fig. 8 shows the procedure developed in this work for the determination of α_c, α_r, β_r, and Λ_c^T. Basically, the procedure is a numerical approach and starts by attributing tentative ranges for the variables α_c, α_r, β_r, and Λ_c^T. As shown in Fig. 8, inside of each specific range the values of the variables α_c, α_r, β_r, and Λ_c^T were varied by loops in a stepwise way from the inferior to superior limits of the ranges. α_c was the outermost loop while β_r was the innermost one. There are two sorts of unknowns in the proposed procedure: the specific range for each one of the variables and the variables themselves. The values attributed to α_c, α_r, β_r, and Λ_c^T in every step of this procedure were tested if they simultaneously satisfy several criteria inside of a specific precision. If so, the set of α_c, α_r, β_r, and Λ_c^T values were considered acceptable values and were written in the output file, otherwise, it was neglected. This procedure was iterated until reach the superior limit of the outermost loop given by α_c. At this point, the set of acceptable values for α_c, α_r, β_r, and Λ_c^T was tested if they obey a normal distribution. If not the range for the variables α_c, α_r, β_r, and Λ_c^T were narrower and the criteria precision were increased. This procedure was repeated several times until the final acceptable criterion precision attained a desirable solution in an almost normal distribution shape.

The criteria and the precision utilized for the variables in the last phase of the algorithm are shown as follow:

Criterion (1). Consider Eq. (46) and make $\rho_c^{IT}(\omega_7) = \rho_c^{IT}(\omega_8)$. This criterion yielded

$$\omega_7\Lambda_c^T - \frac{\beta_r}{\omega_7 - \alpha_r} = \omega_8\Lambda_c^T - \frac{\beta_r}{\omega_8 - \alpha_r}. \tag{73}$$

The acceptability criterion was

$$\left|\frac{\rho_c^*(\omega_7) - \rho_c^*(\omega_8)}{\rho_c^*(\omega_7)}\right| < 0.02, \tag{74}$$

where 0.02 is the relative error,

$$\rho_c^*(\omega_7) = \omega_7\Lambda_c^T - \frac{\beta_r}{\omega_7 - \alpha_r}, \tag{75}$$

and

$$\rho_c^*(\omega_8) = \omega_8\Lambda_c^T - \frac{\beta_r}{\omega_8 - \alpha_r}. \tag{76}$$

Criterion (2) The calculated anticorrelated condition A_{calc} as a function the variables α_c, α_r, β_r, and Λ_c^T was given by Eq. (62). The experimental anticorrelated condition was

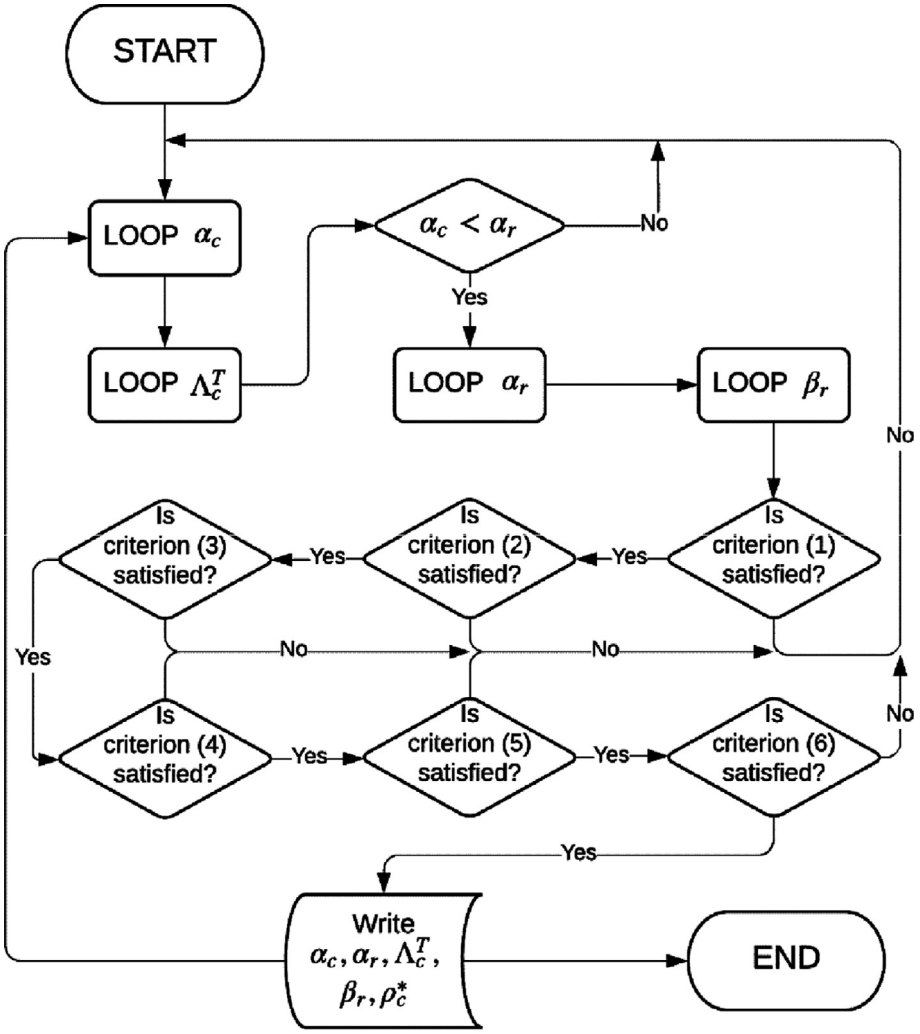

Fig. 8. Flowchart to calculate the distributions for α_c, α_r, β_r, and Λ_c^T.

$$A_{exp} = -\frac{A_7}{A_8}, \tag{77}$$

utilizing the data shown in Fig. 4 yielded $A_{exp} = 0.966$ and $\sigma_{A_{exp}} = 0.026$. The acceptability criterion was

$$\left|A_{exp} - A_{calc}\right| < 3\sigma_{A_{exp}}. \tag{78}$$

Criterion (3) The calculated thermal core generation time $\left(\Lambda^T_{c\,calc}\right)$ employed Eq. (52). The loop that attributed values for thermal core generation time was indicated by $\Lambda^T_{c\,loop}$. The acceptability criterion for this special case was

$$\left|\frac{\Lambda^T_{c\,calc} - \Lambda^T_{c\,loop}}{\Lambda^T_{c\,loop}}\right| < 0.02. \tag{79}$$

Criterion 4) This criterion employed the measured root of the Inhour equation. The Experimental value is shown in Fig. 4, where $\omega_7^{exp} = -2490Hz$ with uncertainty $\sigma_{\omega_7^{exp}} = 11Hz$. Eq. (56) with the positive signal was employed to calculate the first root. This was designated as ω_7^{calc}. The acceptability criterion was

$$\left|\omega_7^{exp} - \omega_7^{calc}\right| < 3\sigma_{\omega_7^{exp}}. \tag{80}$$

Criterion 5) It was done in a similar way to the previous criterion, but with the negative signal in Eq. (56) to calculate the ω_8^{calc}. The experimental value was $\omega_8^{exp} = -6438Hz$ associated with the uncertainty $\sigma_{\omega_8^{exp}} = 132$, as shown in Fig. 4. The acceptability criterion was

$$\left|\omega_8^{exp} - \omega_8^{calc}\right| < 3\sigma_{\omega_8^{exp}}. \tag{81}$$

Criterion 6) Eq. (61) was employed to calculate α_c^{calc}. α_c^{loop} was the value attributed by the loop. The acceptability criterion for this special case was

$$\left|\frac{\alpha_c^{calc} - \alpha_c^{loop}}{\alpha_c^{calc}}\right| < 0.02. \tag{82}$$

The proposed procedure to obtain α_c, α_r, β_r, and Λ_c^T was successfully implemented. Except for the β_r histogram, all other thermal constants follow a normal distribution. Fig. 9 shows an example of the final histogram for the prompt neutron decay constant in the core (α_c). The other thermal quantities (α_r and Λ_c^T) showed similar behavior. This finding makes the whole procedure valid because the histograms do not show any specific tendency or bias. Also, it must be noted that the average value of the distributions corresponds to the maximum of the normal distributions.

The average values of α_c, α_r, β_r, and Λ_c^T arising from the proposed procedure were used as initial guesses in a least-squares approach employing in the ROOT program. The fitting employed the APSD experimental data of the 286.8 ppm of natural boron. The most probable values (averages) were used as initial guesses because several true values could be calculated by the fit program. Therefore, the averages of the distributions were the best initial guesses for the ROOT program to calculate the standard deviations and correlation matrices of the fitted parameters. The constants A_j, ω_9, and ω_{10} of Eq. (2) were fixed, but the roots ω_7 and ω_8 were replaced by Eq. (58). The least-squares procedure with the most probable values of α_c, α_r, β_r, and Λ_c^T converged in a single iteration, thus demonstrating that the adopted procedure to infer these parameters was successful and accurate. The final values along with their uncertainties are given in Table 2.

The correlation matrix is shown in Table 3. According to (Devore, 2014), the correlation will be classified as strong if the absolute value of the correlation coefficients are greater than 0.8, moderate if it lies between 0.5 and 0.8, and weak if it is lower than 0.5. It shows that α_c and α_r are anticorrelated with a relatively strong correlation coefficient. Also, Λ_c^T and β_r have a moderate correlation coefficient. The correlation among the other variables are classified as weak.

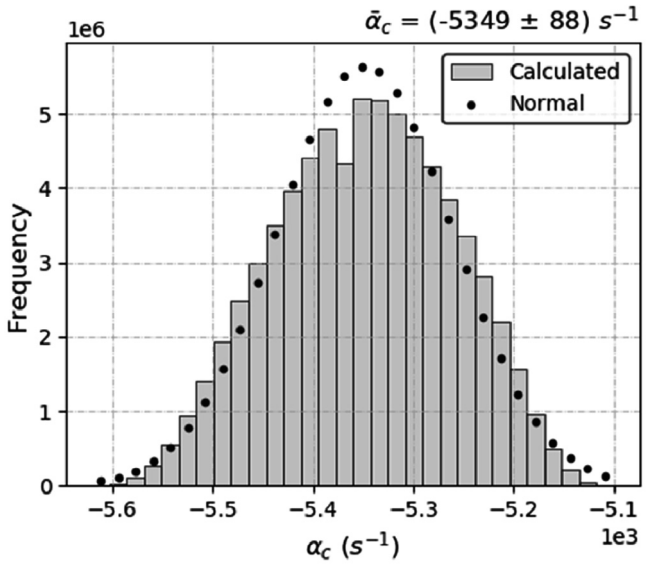

Fig. 9. Final α_c Histogram and its average value.

Table 2
The goodness of fit and the final values of α_c, α_r, β_r, and Λ_c^T.

Parameter	Value
Reduced χ^2	0.99963
Prob (%)	51.49
$\boldsymbol{\alpha_c}(\boldsymbol{s^{-1}})$	−5,348 ± 54
$\boldsymbol{\alpha_r}(\boldsymbol{s^{-1}})$	−3,581 ± 40
$\boldsymbol{\beta_r}(\boldsymbol{s^{-1}})$	63.4 ± 1.9
$\Lambda_c^T(\boldsymbol{\mu s})$	20.35 ± 0.59

5.2. The inference of ρ_c^{TT}, ρ_r^{TT}, $j_{c\to r}^T$, $j_{r\to c}^T$, and Λ_r^T

The quantities ρ_c^{TT}, ρ_r^{TT}, $j_{c\to r}^T$, $j_{r\to c}^T$, and Λ_r^T were determined by using a procedure similar to that described in the previous section. The algorithm is shown in Fig. 10. The fitted values of ω_7, ω_8, α_c, α_r, β_r, and Λ_c^T (Fig. 4 and Table 2) are functions of ρ_c^{TT}, ρ_r^{TT}, $j_{c\to r}^T$, $j_{r\to c}^T$, and Λ_r^T and they were used as constraints in the calculation procedure of this work. An additional condition employed in this section was to get the total reactivity (ρ) from another experiment (dos Santos et al., 2019). After several attempts to calculate ρ, it was found out that this quantity could not be obtained from the set of equations derived in Section 4. The value employed was

$$\rho = -0.06772 \pm 0.00146$$

The criteria utilized for the variables in this last phase of the algorithm are shown below:

Criterion (1). Root ω_7 could be calculated by employing Eq. (48) as:

$$\omega_7^{calc} = \frac{\rho_r^{TT}}{\Lambda_r^T} - \frac{\left[(\omega_7 - \alpha_c)\Lambda_c^T - j_{c\to r}^T\right](\omega_7 - \alpha_r)}{j_{c\to r}^T}, \tag{83}$$

where ω_7^{calc} is the calculated value of ω_7. Criterion (1) was

Table 3
Correlation matrix for the parameters α_c, α_r, β_r, and Λ_c^T.

	α_c	α_r	β_r	Λ_c^T
α_c	1	−0.75676	0.20569	−0.19324
α_r	−0.75676	1	−0.39314	0.38230
β_r	0.20569	−0.39314	1	0.65473
Λ_c^T	−0.19324	0.38230	0.65473	1

$$\left|\omega_7^{exp}-\omega_7^{calc}\right|<2\sigma_{\omega_7^{exp}}, \tag{84}$$

being the experimental value $\omega_7^{exp}=-2490\ s^{-1}$ and its uncertainty $\sigma_{\omega_7^{exp}}=11\ s^{-1}$, as given in Fig. 4.

Criterion (2) Similarly as the previous criterion, the root ω_8 could be calculated as:

$$\omega_8^{calc}=\frac{\rho_r^{TT}}{\Lambda_r^T}-\frac{\left[(\omega_8-\alpha_c)\Lambda_c^T-j_{c\to r}^T\right](\omega_8-\alpha_r)}{j_{c\to r}^T}, \tag{85}$$

where ω_8^{calc} is the calculated value of ω_8. Criterion (2) was

$$\left|\omega_8^{exp}-\omega_8^{calc}\right|<0.1\sigma_{\omega_8^{exp}}, \tag{86}$$

being the experimental value $\omega_8^{exp}=-6438\ s^{-1}$ and its uncertainty $\sigma_{\omega_8^{exp}}=132\ s^{-1}$, as given in Fig. 4.

Criterion (3) α_r could be calculated with Eq. (60) and employing ω_7^{exp} given previously. The criterion (3) was

$$\left|\alpha_r^{exp}-\alpha_r^{calc}\right|<\sigma_{\alpha_r^{exp}}, \tag{87}$$

where the experimental value is $\alpha_r^{exp}=-3581\ s^{-1}$ and its uncertainty is $\sigma_{\alpha_r^{exp}}=40\ s^{-1}$, as in Table 2.

Criterion (4) α_r could be calculated employing Eq. (60) with ω_8^{exp}. Criterion (4) was

$$\left|\alpha_r^{exp}-\alpha_r^{calc}\right|<\sigma_{\alpha_r^{exp}}, \tag{88}$$

where the experimental value is $\alpha_r^{exp}=-3581\ s^{-1}$ and its uncertainty is $\sigma_{\alpha_r^{exp}}=40\ s^{-1}$, as in Table 2.

Criterion (5)α_r could be calculated employing Eq. (38), obtaining α_r^{calc}. Criterion (5) was

$$\left|\alpha_r^{exp}-\alpha_r^{calc}\right|<2\sigma_{\alpha_r^{exp}}, \tag{89}$$

where α_r^{exp} and its corresponding uncertainty is given above.

Criterion (6)β_r could be calculated employing Eq. (39). Criterion (6) was

$$\left|\beta_r^{exp}-\beta_r^{calc}\right|<2\sigma_{\beta_r^{exp}}, \tag{90}$$

where the experimental value is $\beta_r^{exp}=-63.4\ s^{-1}$ and its uncertainty is $\sigma_{\beta_r^{exp}}=1.9\ s^{-1}$, as in Table 2.

Criterion (7) The total thermal reactivity is given by Eq. (49), resulting in the criterion (7) which was given by

$$\left|\rho_{exp}-\rho_{calc}\right|<2\sigma_{\rho_{exp}^{TT}}, \tag{91}$$

where ρ_{calc} is the calculated value, the experimental value is $\rho_{exp}=-0.06772$ and its uncertainty is $\sigma_{\rho_{exp}}=0.00146$.

Criterion (8) This criterion was

$$\left|F_{exp}-F_{calc}\right|<2\sigma_{F_{exp}}, \tag{92}$$

where the calculated quantity was obtained from Eq. (37) and it was given by:

$$F_{calc}=\rho_c^{TT}-j_{c\to r}^T. \tag{93}$$

F_{exp} was determined as:

$$F_{exp}=\alpha_c\Lambda_c^T+\beta_{eff}^{TF}, \tag{94}$$

where, from the data of Table 2, $F_{exp}=-0.1021$ and its uncertainty is $\sigma_{\rho_{exp}^{TT}}=0.0035$.

Criterion (9) This criterion was obtained from Eq. (40). After some manipulations:

$$G_{calc}=\rho_c^{TT}-\frac{\left(\omega_7\Lambda_r^T-\rho_r^{TT}\right)j_{c\to r}^T}{\omega_7\Lambda_r^T-\rho_r^{TT}+j_{r\to c}^T}. \tag{95}$$

G_{exp} was given by:

$$G_{exp}=\omega_7\Lambda_c^T+\beta_{eff}^{TF}. \tag{96}$$

Criterion (9) could be written as:

$$\left|G_{exp}-G_{calc}\right|<2\sigma_{G_{exp}}, \tag{97}$$

where $G_{exp}=-0.0439$ and its uncertainty is $\sigma_{G_{exp}}=0.0015$.

Criterion (10) Similar to the previous criterion, the calculated unknown given by

$$H_{calc}=\rho_c^{TT}-\frac{\left(\omega_8\Lambda_r^T-\rho_r^{TT}\right)j_{c\to r}^T}{\omega_8\Lambda_r^T-\rho_r^{TT}+j_{r\to c}^T}, \tag{98}$$

and the experimental one by

$$H_{exp}=\omega_8\Lambda_c^T+\beta_{eff}^{TF}. \tag{99}$$

The criterion (10) is

$$\left|H_{exp}-H_{calc}\right|<2\sigma_{H_{exp}}, \tag{100}$$

where $H_{exp}=-0.1243$ and its uncertainty is $\sigma_{H_{exp}}=0.0047$.

All histograms for the thermal constants ρ_c^{TT}, ρ_r^{TT}, $j_{c\to r}^T$, $j_{r\to c}^T$, and Λ_r^T, which simultaneously satisfied the criteria shown previously, follow a normal distribution. Similarly to the cases of α_c, α_r, β_r, and Λ_c^T, these averages values were used as initial guesses in a least-squares approach employing the ROOT program. The constants A_j, ω_9, and ω_{10} of Eq. (2) were fixed again, but the roots ω_7 and ω_8 were replaced by Eq. (59). The least-squares procedure with the most probable values of ρ_c^{TT}, ρ_r^{TT}, $j_{c\to r}^T$, $j_{r\to c}^T$, and Λ_r^T converged in a single iteration, thus demonstrating that the adopted procedure was successful and accurate. The final values along with their uncertainties are given in Table 4.

The correlation matrix is shown in Table 5. Here, it shows that Λ_r^T and ρ_r^{TT} are anticorrelated and their correlation coefficient is very close to being classified as strong. The other variables show a weak correlation (Devore, 2014).

5.3. Determination of the lifetimes

Section 4.3 shows two ways to get the thermal neutron lifetime. Here, the numerical values of this quantity are presented along with their uncertainty. Table 6 shows these values.

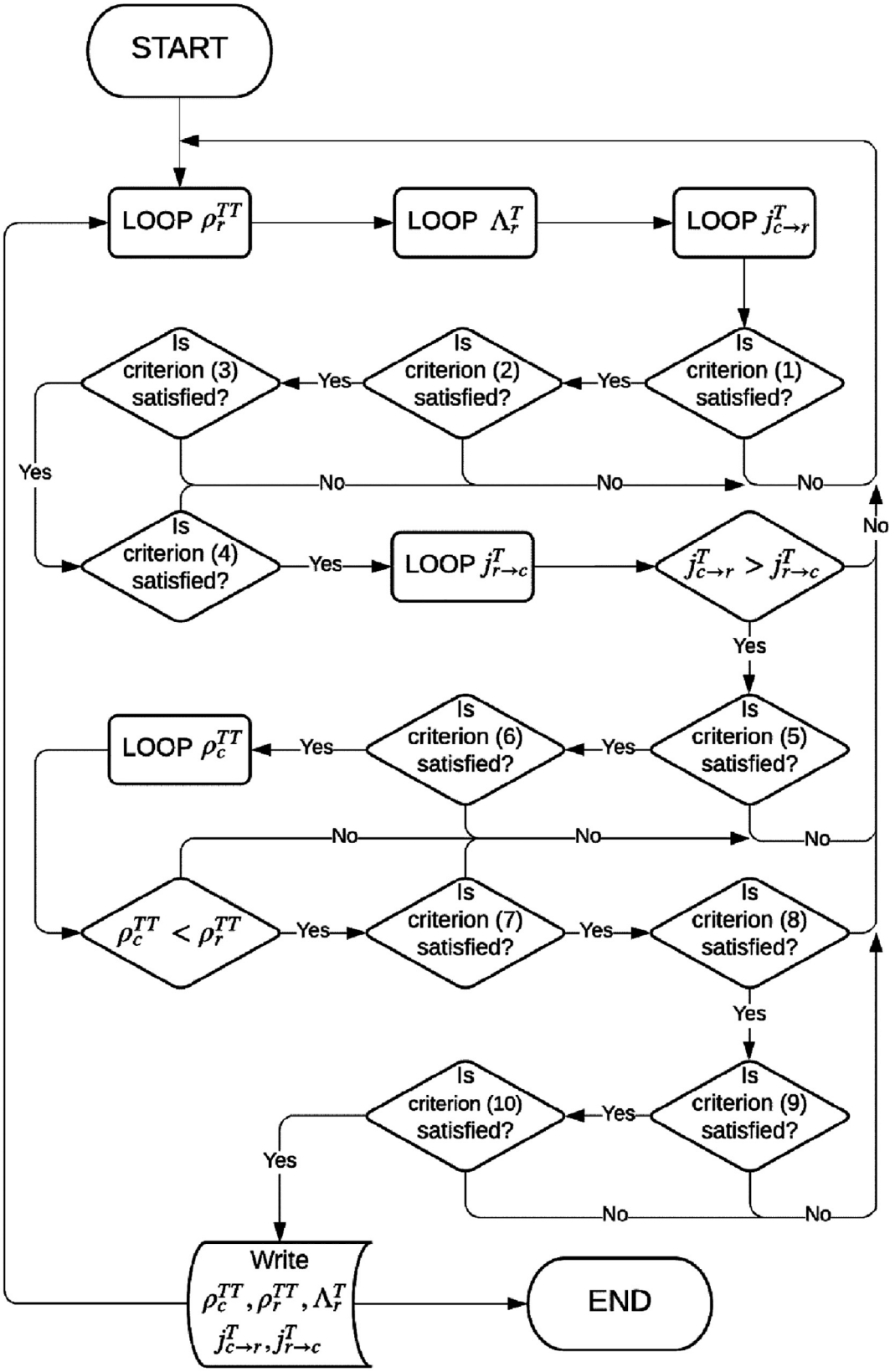

Fig. 10. Flowchart to calculate the distributions of ρ_c^{TT}, ρ_r^{TT}, $j_{c\to r}^T$, $j_{r\to c}^T$, and Λ_r^T.

Table 4
The goodness of fit and the final values of ρ_c^{TT}, ρ_r^{TT}, $j_{c\to r}^{T}$, $j_{r\to c}^{T}$, and Λ_r^T.

Parameter	Value
Reduced χ^2	0.99967
Prob (%)	51.31
$\boldsymbol{\rho_c^{TT}}$	−0.05336 ± 0.00050
$\boldsymbol{\rho_r^{TT}}$	−0.01556 ± 0.00055
$\boldsymbol{j_{c\to r}^{T}}$	0.04966 ± 0.00080
$\boldsymbol{j_{r\to c}^{T}}$	0.00936 ± 0.00023
$\Lambda_r^T(\boldsymbol{\mu s})$	6.96 ± 0.14

6. Theoretical results and comparison to experiments

Many of the inferred quantities reported previously are not determined by the several reactor codes available today. The theory/experiment comparisons shown are only for the quantities ρ_c^{TT}, ρ_r^{TT}, ρ, Λ^T and τ^T, and they will be done in an approximated way. Particularly, $\rho_c^{TT}$and ρ_r^{TT} reactivity variations are assumed to be independent of each other. The correct way of making these comparisons is to employ equations (25) and (29) and to perform the integrals together with the direct and adjoint fluxes. The theory/experiments comparisons of the thermal prompt neutron generation time (Λ^T) and the thermal lifetime (τ^T) will also be performed in an approximated way since the thermal energy cutoff is not well defined in the experiments.

The theoretical analyses of the experiment were performed employing MCNP6 (Goorley et al., 2013) in conjunction with ENDF/B-VII.0 (Chadwick et al., 2006) and JENDL 3.3 (Shibata et al., 2002) nuclear data libraries. The nuclear data of ^{235}U and ^{238}U were taken from JENDL 3.3 and the remainders from ENDF/B-VII.0. The main reason for the utilization of JENDL 3.3 nu clear data was its best nuclear data for the delayed neutrons, as described in (dos Santos and Diniz, 2014).

The radial and axial geometric models follow closely the several benchmark models of the IPEN/MB-01 reactor (dos Santos et al., 2014, 2006b) available in the IRPhE handbook. The radial model is based in a rectangular array of 26 × 24 fuel rods immersed in a light water tank. The control and safety banks were considered totally withdrawn. The major distinction here is the utilization of boric acid in the reactor water and the separation of the core and reflector region.

All MCNP6 cases requested a KCODE calculation employing 2×10^5 histories per cycle. A total of 1000 cycles was employed and the first 20 cycles were skipped.

Table 7 shows the calculated k_{eff} and the relative reactivity ($\Delta\rho$) for the 4 cases simulated by MCNP6 for the experiment considered in this work. The notation "Water" means that the moderator water was not poisoned with boric acid. The notation "286.8 ppm" means that the moderator water was poisoned with 286.8 ppm of natural boron. The boron poisoning was done in both core and reflector regions or in just one of these regions, as shown in Table 7. The core is the region that contains the 26 × 24 fuel rods array. The pitch of the facility is 1.50 cm and the radial size of the core is 39 × 36 cm. Its height is the height of the fuel region, which is 54.84 cm. The reflector region is all other regions that complement the reactor model.

Table 6
Experimental thermal neutron lifetime.

Lifetime	Equation
$\tau^T = (25.55 \pm 0.57)\mu s$	(67)
$\tau^T = (25.89 \pm 0.24)\mu s$	(72)

The reference simulation (case 1) in Table 7 is the configuration with water in the two regions. Its measured reactivity excess was $\Delta\rho = (10 \pm 3)$ *pcm* and the calculated reactivity between case 1 (reference) and $k_{eff} = 1$ was $\Delta\rho = (-83 \pm 5)$ *pcm*. JENDL-3.3 library underestimated the value of k_{eff} in approximately 100 pcm. Even so, the calculated reactivities showed excellent estimates compared to the experimental ones.

All reactivity variations $\Delta\rho(pcm)$ shown in Table 7 are calculated relative to case 1 (the reference case). The hypotheses of making ρ_r^{TT} and ρ_c^{TT} independent of each other are made assuming that these two quantities are, respectively, given by the reactivity variations of cases 2 and 3. The total reactivity variation, given by case 4, is more reliable for a comparison between theory and experiment.

Table 8 shows the calculated generation time (Λ), β_{eff}, removal time (t_{rem}), and lifetime (τ). t_{rem} is the nonadjoint lifetime and τ is the adjoint lifetime calculated by Eq. (67). The simulations considered the total energy spectrum, indicated by "Total", and a cutoff that eliminated the neutrons below 1 eV ($E > 1eV$), producing quantities related to fast neutrons. Cases 1 and 4 show that β_{eff} in the total neutron energy change little with decreasing reactivity, as assumed in the first hypothesis mentioned before. The thermal generation time $\Lambda^T$and the thermal lifetime $\boldsymbol{\tau^T}$ can be found subtracting the corresponding results of case 4 in the "Total" case and in the "cutoff" case.

The comparisons between generation times and lifetimes were restricted to the values for the whole reactor systems. Table 9 presents the calculated-to-measured comparison. The experimental τ^T is the average of the two values of Table 6. Except for ρ_r^{TT}, all other calculated quantities showed good agreements inside 3σ range of the total uncertainty. The great difference in ρ_r^{TT} might be credited to the way that this reactivity was calculated. The MCNP6 models for the determination of $\rho_c^{TT}$and ρ_r^{TT} assume their independence of each other. This hypothesis might be more restrictive for the ρ_r^{TT} determination than that for ρ_c^{TT}.

Table 5
Correlation matrix for the parameters ρ_c^{TT}, ρ_r^{TT}, $j_{c\to r}^{T}$, $j_{r\to c}^{T}$, and Λ_r^T.

	$\boldsymbol{\rho_c^{TT}}$	$\boldsymbol{\rho_r^{TT}}$	$\boldsymbol{j_{c\to r}^{T}}$	$\boldsymbol{j_{r\to c}^{T}}$	Λ_r^T
$\boldsymbol{\rho_c^{TT}}$	1	−0.35012	0.46867	−0.35654	0.25923
$\boldsymbol{\rho_r^{TT}}$	−0.35012	1	0.34492	0.19493	−0.79027
$\boldsymbol{j_{c\to r}^{T}}$	0.46867	0.34492	1	0.35816	−0.2526
$\boldsymbol{j_{r\to c}^{T}}$	−0.35654	0.19493	0.35816	1	0.25832
Λ_r^T	0.25923	−0.79027	−0.2526	0.25832	1

Table 7
k_{eff} and $\Delta\rho$ for the MCNP6 simulations.

Case	Core	Reflector	k_{eff}	$\Delta\rho(pcm)$
1	Water	Water	0.99917 ± 0.00005	Reference
2	Water	286.8 ppm	0.98702 ± 0.00005	-1232 ± 7
3	286.8 ppm	Water	0.94755 ± 0.00005	-5452 ± 7
4	286.8 ppm	286.8 ppm	0.93636 ± 0.00005	-6713 ± 8

Table 8
Λ, β_{eff}, t_{rem}, and τ for the MCNP6 simulations.

Case	Energy	$\Lambda(\mu s)$	$\beta_{eff}(pcm)$	$t_{rem}(\mu s)$	$\tau(\mu s)$
1	Total	31.637 ± 0.036	762 ± 7	64.7	31.611 ± 0.036
4	Total	29.203 ± 0.030	760 ± 7	47.7	27.345 ± 0.028
4	$E > 1eV$	3.362 ± 0.007	758 ± 11	0.822	0.4254 ± 0.009

Table 9
Theory/Experiment comparisons.

Quantity	Experimental (E)	Calculated (C)	$C/E - 1$
$\rho_c^{TT}(pcm)$	-5336 ± 50	-5452 ± 7	$(2.2 \pm 1,0)\%$
$\rho_r^{TT}(pcm)$	-1556 ± 55	-1232 ± 7	$(20.8 \pm 2.8)\%$
$\rho(pcm)$	-6892 ± 61	-6713 ± 8	$(2.6 \pm 1.1)\%$
$\Lambda^T(\mu s)$	27.31 ± 0.61	25.841 ± 0.031	$(5.4 \pm 2.1)\%$
$\tau^T(\mu s)$	25.72 ± 0.62	26.919 ± 0.028	$(4.7 \pm 2.5)\%$

7. Conclusions

The subcritical experiment for the APSD measurements at frequencies up to 100 kHz has been successfully performed at the IPEN/MB-01 reactor. The experiment was very challenging because it required a long acquisition time and it was very sensitive to the electronic setup. The analyses revealed that the APSD modes occur in pairs and, the higher the frequency, the more pairs of modes could be solved. The APSD measurement data reached the best statistical qualities of a good fit in a four-mode model. If the measurements went beyond 100 kHz, it would be possible to fit more pairs of modes. In the four-mode fit, it was demonstrated that there were two distinct frequencies regions, as exposed in the individual modes of the case of 286.8 ppm of natural boron shown in Fig. 6. The first two modes dominated the lower frequency region, while the last two dominated the higher one. The physical interpretation was that the first two modes corresponded to the thermal neutron group and the last two to the fast neutron group. The coupling of these pairs of modes was weak, therefore, they could be considered uncoupled in the theoretical model.

The recent neutron kinetic models (Dulla et al., 2006; Gandini, 2004; 2001;; Sugawara et al., 2012) and even the two-region kinetic model of Spriggs (Spriggs et al., 1997) could not explain the experimental data. For this reason, a theoretical two-group two-region kinetic model was developed starting from the neutron transport equations and considering the interpretation of the measurements. In this model, the thermal group was completely solved and employed for the inference of several parameters of interest in the reactor physics area. Only the case of 286.8 ppm of natural boron was analyzed and the subcritical reactivities ρ_c^{TT}, ρ_r^{TT}, and ρ, the neutron generation times Λ_c^T, Λ_r^T , and Λ^T, the lifetime τ^T, α_c, and α_r could be inferred from the experimental data in a high degree of accuracy. During the process, the quantities β_r, $j_{c\to r}^T$, and $j_{r\to c}^T$ were also obtained.

The theory-to-experiment comparison was performed only for the case of 286.8 ppm of natural boron and employed MCNP6 in conjunction with ENDF/B-VII.0 and JENDL 3.3 nuclear data libraries. The comparison reveals that the values of ρ_c^{TT}, ρ, Λ^T, and τ^T agreed within 3σ, but ρ_r^{TT} shows some discrepancy.

In general, the experimental data are of excellent quality and suitable for an international benchmark, since the entire experimental procedure was carefully performed, as described in the reference (dos Santos, 2020). Several important thermal constants for the kinetic behavior of the IPEN/MB-01 reactor such as the prompt neutron decay constant (α_c and α_r), the partial reactivity ($\rho_c^{TT}$and ρ_r^{TT}), and the prompt neutron generation time (Λ_c^T. and Λ_r^T) all in the core and reflector were experimentally determined for the first time. The data can be useful for the validation of neutron cross-section libraries employed in the simulation programs.

Declaration of Competing Interest

The authors declare that they have no known competing financial interests or personal relationships that could have appeared to influence the work reported in this paper.

Acknowledgments

The authors would like to thank the nuclear reactor operators from the IPEN/MB-01 nuclear facility for all support in the experiments. The first author would like to thank the professors Adimir dos Santos for all teachings.

References

Avery, R., Branyan, C.E., Brunson, G.S., Cohn, C.E., Fischer, G.F., Hummel, H.H., Kato, W.Y., Kirn, F.S., Meneghetti, D., Thalgott, F.W., Toppel, B.J., 1958. Coupled fast-thermal power breeder critical experiment, in: Proc. 2nd. Intern. Conf. Peaceful Uses Atomic Energy. p. V.12, 151.

Bell, G.I.I., Glasstone, S., 1970. Nuclear Reactor Theory. Van Nostrand Reinhold Company, Van Nostrand Reinhold, New York.

Bess, J.D., Briggs, J.B., Ivanova, T., Hill, I., Gulliford, J., 2017. Availability of Neutronics Benchmarks in the ICSBEP and IRPhEP Handbooks for Computational Tools Testing, in: International Conference on Mathematics & Computational Methods Applied to Nuclear Science & Engineering (M&C 2017) INL/CON-16-40129. Idaho National Lab. (INL).

Blaise, P., Mellier, F., Fougeras, P., 2011. Application of the Modified Source Multiplication (MSM) Technique to Subcritical Reactivity Worth Measurements in Thermal and Fast Reactor Systems. IEEE Trans. Nucl. Sci. 58, 1166–1176. https://doi.org/10.1109/TNS.2011.2115254.

Chadwick, M.B., Oblozinskı, P., Herman, M., Greene, N.M., McKnight, R.D., Smith, D. L., Young, P.G., MacFarlane, R.E., Hale, G.M., Frankle, S.C., 2006. ENDF/B-VII.0: Next generation evaluated nuclear data library for nuclear science and technology. Nucl. Data Sheets 107, 2931–3060. https://doi.org/10.1016/j.nds.2006.11.001.

Cohn, C.E., 1962. Reflected-Reactor Kinetics. Nucl. Sci. Eng. 13.

de Hoffmann, F., 1949. Statistical aspects of pile theory, in: Ed. Goodman, C.D. (Ed.), Science and Engineering on Nuclear Power, Vol. II. Addison-Wesley, Mass.

Devore, J.L., 2014. Probability and statistics for engineering and the sciences. Cengage Learning, Boston, USA.

Diniz, R., dos Santos, A., 2006. Experimental Determination of the Decay Constants and Abundances of Delayed Neutrons by Means of Reactor Noise Analysis. Nucl. Sci. Eng. 152, 125–141. https://doi.org/10.13182/nse04-69.

dos Santos, A., Diniz, R., 2014. The evaluation of the effective kinetic parameters and reactivity of the IPEN/MB-01 reactor for the international reactor physics experiment evaluation project. Nucl. Sci. Eng. 178, 459–478. https://doi.org/10.13182/NSE14-10.

dos Santos, A., Diniz, R., Fanaro, L.C.C.B., Jerez, R., Silva, G.S., de, A., Yamaguchi, M., 2006a. A proposal of a benchmark for βeff, βeff/Λ, and Λ of thermal reactors fueled with slightly enriched uranium. Ann. Nucl. Energy 33, 848–855. https://doi.org/10.1016/j.anucene.2006.03.006.

dos Santos, A., Lee, S., Diniz, R., Jerez, R., 2013. A New Experimental Approach for Subcritical Reactivity Determination of Multiplying Systems. Ann. Nucl. Energy 59, 243–254. https://doi.org/10.1016/j.anucene.2013.04.015.

dos Santos, A., Silva, Graciete Simões, de Andrade Fanaro, L.C.C.B., Yamaguchi, M., Jerez, R., Diniz, R., Kuramoto, R.Y.R., 2012. IPEN (MB01)-LWR-COEF-KIN-RESR-001: Reactor Physics experiments in the IPEN/MB-01 Research Reactor Facility. International Handbook of Evaluated Reactor Physics Benchmark Experiments, Paris NEA/NSC, pp. 1–142.

dos Santos, A., Silva, G.S. de A., Fanaro, L.C.C.B., Yamaguchi, M., Jerez, R., 2014. LEU-COMP-THERM-077: Critical Loading Configurations of the IPEN/MB-01 Reactor. In: Briggs, J. Blair (Ed.), in: International Handbook of Evaluated Criticality Safety Benchmark Experiments. NEA/NSC/DOC (95)03/I, Paris.

dos Santos, A., Silva, G.S. de A., Fanaro, L.C.C.B., Yamaguchi, M., Jerez, R., Diniz, R., Carneiro, Á.L.G., Kuramoto, R.Y.R., Mendonça, A.G., Fuga, R., Maeda, R. de M., Mura, L.F.L., 2006b. IPEN(MB01)-LWR-RESR-001 CRIT-BUCK-SPEC-REAC-COEF-KIN-RRATE-POWDIS REACTOR: Reactor Physics Experiments in the IPEN/MB-01 Research Reactor Facility, in: International Handbook of Evaluated Reactor Physics Benchmark Experiments. NEA/NSC/DOC/(2006)1.

dos Santos, A., Souza, G.S. de, Santos, D.F. dos, de Andrade e Silva, G.S., 2019. Subcritical boron experiments in the IPEN/MB-01 reactor, in: European Nuclear Society (Ed.), RRFM European Research Reactor Conference. Brussels, Belgium..

Dulla, S., Ravetto, P., Carta, M., Angelo, A., 2006. Kinetic Parameters for Source Driven Systems, in: PHYSOR-2006. ANS Topical Meeting on Reactor Physics Organized and Hosted by the Canadian Nuclear Society. Vancouver, BC, Canada.

Feynman, R.P., de Hoffmann, F., Serber, R., 1956. Dispersion of the neutron emission in U-235 fission. J. Nucl. Energy 3, 64–69.

Gajda, P., Janczyszyn, J., Pohorecki, W., 2013. Correction methods for pulsed neutron source reactivity measurement in accelerator driven systems. Nukleonika 58, 287–293.

Gandini, A., 2004. ADS subcriticality evaluation based on the generalized reactivity concept. Ann. Nucl. Energy 31, 813–821. https://doi.org/10.1016/j.anucene.2003.10.008.

Gandini, A., 2001. HGPT Based Sensitivity Time-Dependent Method for the Analysis of Subcritical Systems. Ann. Nucl. Energy 28, 1193–1217.

Gonnelli, E., dos Santos, A., 2016. The Determination of Reflector Kinetics Parameters Through Rossi-α Experiments in the IPEN/MB-01 Reactor, in: PHYSOR. Sun Valley, Idaho, USA.

Goorley, J.T., James, M.R., Booth, T.E., Brown, F.B., Bull, J.S., Cox, L.J., Durkee, J.W., Elson, J.S., Fensin, M.L., Forster, R.A., Hendricks, J.S., Hughes, H.G., Johns, R.C., Kiedrowski, B.C., Mashnik, S.G., Mckinney, G.W., Pelowitz, D.B., Prael, R.E., Sweezy, J.E., Waters, L.S., Wilcox, T.A., Zukaitis, A., 2013. MCNP6 User's Manual Version 1.0, Los Alamos National Laboratory. Los Alamos National Laboratory, Los Alamos, New Mexico.

IAEA, 2013. International Atomic Energy Agency (IAEA). Research Reactors: Purpose and Future. URL: http://www.iaea.org/OurWork/ST/NE/NEFW/Technical_Areas/RRS/documents/RR_Purpose_and_Future_BODY.pdf (accessed 02.06.20).

Keysight Technologies Inc. 2017. Keysight 35670A Dynamic Signal Analyzer. URL: https://www.keysight.com/us/en/assets/7018-06736/technical-overviews/5966-3063.pdf (accessed 07.01.20).

Kitamura, Y., Matoba, M., Misawa, T., Unesaki, H., Shiroya, S., 1999. Reactor noise experiments by using acquisition system for time series data of pulse train. J. Nucl. Sci. Technol. 36, 653–660. https://doi.org/10.1080/18811248.1999.9726252.

Knoll, G.F., 2000. Radiation detection and measurement. John Wiley & Sons Inc, New York.

Kobayashi, K., 1990. Rigorous derivation of static and kinetic nodal equations for coupled reactors using transport equation. Nucl. Sci. Technol. 28, 389–398.

Kumar, R., Degweker, S.B., Singh, K.P., Ali, M.Y., 2016. Measurement of sub-critical reactivity in a heavy water reactor by neutron noise methods using a time stamping data acquisition system. Ann. Nucl. Energy 87, 720–727. https://doi.org/10.1016/j.anucene.2015.06.046.

Kuramoto, R.Y.R., dos Santos, A., Diniz, R., Jerez, R., 2008. Absolute Measurement of βeff based on Rossi-α experiments and the Two-Region Model in the IPEN/MB-01 Research Reactor. Nucl. Sci. Eng. 158, 272–283. https://doi.org/10.13182/NSE06-120.

Kuramoto, R.Y.R., dos Santos, A., Jerez, R., Diniz, R., 2007. Absolute Measurement of βeff based on Feynman-α experiments and the Two-Region Model in the IPEN/MB-01 Research Reactor. Ann. Nucl. Energy 34, 433–442. https://doi.org/10.1016/j.anucene.2007.02.012.

Lamarsh, J.R., 1966. Introduction to nuclear reactor theory. Addison-Wesley Publising Company, inc., Massachusetts, EUA.

Mihalczo, J.T., Blakeman, E.D., Ragan, G.E., Johnson, E.B., Hachiya, Y., 1990. Dynamic Subcriticality Measurements Using the 252Cf-Source-Driven Noise Analysis Method. Nucl. Sci. Eng. 104, 314–338. https://doi.org/10.13182/nse90-a23732.

Misawa, T., Unesaki, H., 2003. Measurement of Subcriticality by Higher Mode Source Multiplication Method, in: JAERI (Ed.), JAERI Conference. Osake, Japan, pp. 178–182.

Moore, M.N., 1959. The power noise transfer function of a reactor. Nucl. Sci. Engng. 6, 448.

Moore, M.N., 1958a. The determination of reactor transfer function from measurements at steady operation. Nucl. Sci. Engng. 3, 387.

Moore, M.N., 1958b. Reactor transfer functions: addendum. Nucl. Sci. Engng. 4, 134.

Nishina, K., Yamane, Y., 1985. A two-group response function treatment of coupled-core kinetics equations and coupling coefficient. Nucl. Sci. Eng. 89, 102.

Orndoff, J.D., 1957. Prompt neutron periods of metal critical assemblies. Nucl. Sci. Enyng. 2, 450.

Saito, K., 1979. Source papers in reactor noise. Prog. Nucl. Energy 3, 157–218. https://doi.org/10.1016/0149-1970(79)90018-0.

Sakon, A., Hashimoto, K., Aiman, M., Maarof, M.A. Bin, Kawasaki, M., Sugiyama, W., Pyeon, C.H., Sano, T., Yagi, T., Ohsawa, T., 2014. Measurement of large negative reactivity of an accelerator-driven system in the Kyoto University Critical Assembly. J. Nucl. Sci. Technol. 51, 116–126. https://doi.org/10.1080/00223131.2013.852488.

Sakon, A., Hashimoto, K., Sugiyama, W., Taninaka, H., Pyeon, C.H., Sano, T., Misawa, T., Unesaki, H., Ohsawa, T., 2013. Power spectral analysis for a thermal subcritical reactor system driven by a pulsed 14 MeV neutron source. J. Nucl. Sci. Technol. 50, 481–492. https://doi.org/10.1080/00223131.2013.785268.

Santos, D.F. dos, 2020. Ruído neutrônico macroscópico até 100 kHz do reator IPEN/MB–01. Doctoral thesis in Portuguese, São Paulo University, São Paulo, Brazil. URL: https://teses.usp.br/index.php?option=com_jumi&fileid=17&Itemid=160&id=87A86E7A0948&lang=pt-br.

Shahbunder, H., Pyeon, C.H., Misawa, T., Shiroya, S., 2010. Experimental analysis for neutron multiplication by using reaction rate distribution in accelerator-driven system. Annals of Nuclear Energy. Ann. Nucl. Energy 37, 592–597. https://doi.org/10.1016/j.anucene.2009.12.022.

Shibata, K., Kawano, T., Nakagawa, T., Iwamoto, O., Ichi Katakura, J., Fukahori, T., Chiba, S., Hasegawa, A., Murata, T., Matsunobu, H., Ohsawa, T., Nakajima, Y., Yoshida, T., Zukeran, A., Kawai, M., Baba, M., Ishikawa, M., Asami, T., Watanabe, T., Igashira, M., Yamamuro, N., Kitazawa, H., Yamano, N., Takano, H., 2002. Japanese evaluated nuclear data library version 3 revision-3: JENDL-3.3. J. Nucl. Sci. Technol. 39, 1125–1136. https://doi.org/10.1080/18811248.2002.9715303.

Shinkawa, M., Yamane, Y., Nishina, K., Tamagawa, H., 1978. Theoretical analysis of coupled-core reactors with the method of the moderator region response function. Nucl. Sci. Eng. 67, 19–33.

Sjöstrand, N.G., 1956. Measurement on a subcritical reactor using a pulsed neutron source. Ark. för Fys. 11.

Soule, R., Bertrand, P., Pont, J., Gauthier, J.C., Granget, G., Avramov, A.M., Doulin, V.A., Zhuravlev, V.I., Kochetkov, A.L., Momontov, V.F., Matveenko, I.P., Mikhailov, J.M., Shokodko, A.J., 1990. The measurement of the effective delayed-neutron fraction in the fast critical assembly BFS with uranium-plutonium metal fuel, in: International Conference on the Physics of Reactors: Operation, Design and Computation (PHYSOR 90). Marseille (France).

Spriggs, G.D., Busch, R.D., 1997. On the definition of neutron lifetimes in multiplying and non-multiplying systems (LA-13260-MS). Brazilian Meet. React. Phys. thermohydraulics. https://doi.org/10.1007/3-540-58184-7_109.

Spriggs, G.D., Busch, R.D., Williams, J.G., 1997. Two-region kinetic model for reflected reactors. Ann. Nucl. Energy 24, 205–250. https://doi.org/10.1016/0306-4549(96)00062-X.

Stillwell, J., 2004. Mathematics and Its History. Springer, San Francisco.

Sugawara, T., Iwasaki, T., Chiba, T., Nishihara, K., 2012. Development of Dynamics Code and Proposal of Start-up Procedure for Accelerator Driven System. J. Nucl. Sci. Technol., 23–31

Suzuki, E., 1966. A Method for Measuring Absolute Reactor Power through Neutron Fluctuation. J. Nucl. Sci. Technol. 3, 98–105. https://doi.org/10.1080/18811248.1966.9732284.

Szieberth, M., Klujber, G., Kloosterman, J.L., Haas, D., 2015. Measurement of multiple α-modes at the Delphi subcritical assembly by neutron noise techniques. Ann. Nucl. Energy 75, 146–157. https://doi.org/10.1016/j.anucene.2014.07.018.

Tsuji, M., Suzuki, N., Shimazu, Y., 2003. Subcriticality measurement by neutron source multiplication method with a fundamental mode extraction. J. Nucl. Sci. Technol. 40, 158–169. https://doi.org/10.1080/18811248.2003.9715346.

Uhrig, R.E., 1970. Random noise techniques in nuclear reactor systems. The Ronald Press Company, Florida.

Van Dam, H., 1996. Inhour equation and kinetic distortion in a two-point reactor kinetic model. Ann. Nucl. Energy 23, 1127–1142.

Wasserman, A.A., 1960. A simple model for the effect of reflected neutrons upon reactor kinetics, Phillips Petroleum Company Quarterly Technical Report- Spert Project, IDO-16606.

Williams, M.M.R., 1974. Random Processes in Nuclear Reactors, Nuclear Science and Engineering. Pergamon Press, Londres.

X-5 Monte Carlo Team, 2008. MCNP - A general Monte Carlo N-Particle transport code, version 5.

Yamane, Y., Tanaka, K., Nishina, K., Tamagawa, H., Shiroya, S., 1980. The determination of coupled-core-reactor kinetics parameters through frequency response. Nucl. Sci. Eng. 76, 232.